Validation of a data-driven fast numerical model to simulate the Immersion Cooling of a Lithium-ion Battery Pack

Elie Solai, Maxime Guadagnini, Heloise Beaugendre, Rémi Daccord, Pietro Marco Congedo

Highlights

Validation of a data-driven fast numerical model to simulate the Immersion Cooling of a Lithium-ion Battery Pack.

Elie SOLAI, Maxime GUADAGNINI, Héloïse BEAUGENDRE, Rémi DACCORD, Pietro CONGEDO

- We develop a data-driven fast numerical model to predict the behavior of the battery pack.
- We provide data of an experimental test case of Li-ion cells immersion cooling.
- We apply Bayesian calibration method to get posterior distributions of input parameters using experimental data.
- Our approach allows reducing the numerical error bar of the model temperature response dramatically.

Validation of a data-driven fast numerical model to simulate the Immersion Cooling of a Lithium-ion Battery Pack.

Elie SOLAI[a,*], Maxime GUADAGNINI[b], Héloïse BEAUGENDRE[a], Rémi DACCORD[b], Pietro CONGEDO[c]

[a]*Inria, Univ. Bordeaux, CNRS, Bordeaux INP, Institut de Mathématiques de Bordeaux, Bordeaux, 33000, France*
[b]*Exoes, ZA Bersol, 6 Av. de la Grande Lande, 33170 Gradignan, France*
[c]*Inria, CMAP, CNRS, Ecole Polytechnique, IPP, Palaiseau, France*

Abstract

Thermal management of Lithium-ion batteries is a key element to the widespread of electric vehicles. In this study, we illustrate the validation of a data-driven numerical method permitting to evaluate fast the behavior of the Immersion Cooling of a Lithium-ion Battery Pack. First, we illustrate an experiment using a set up of immersion cooling battery pack, where the temperatures, voltage and electrical current evolution of the Li-ion batteries are monitored. The impact of different charging/discharging cycles on the thermal behavior of the battery pack is investigated. Secondly, we introduce a numerical model, that simulates the heat transfer and electrical behavior of an immersion cooling Battery Thermal Management System. The deterministic numerical model is compared against the experimental measurements of temperatures. Then, we perform a Bayesian calibration of the multi-physics input parameters using the experimental measurements directly. The informative distributions outcoming of this process are used to validate the model in different experimental conditions and reduce the uncertainty in the model's temperatures predictions. Finally, the learned distributions of inputs and the numerical model are used to design the system under realistic conditions representing a realistic racing car operation. A Sobol indices based sensitivity analysis is performed to get further analysis elements on the behavior of the BTMS.

Keywords: Lithium-ion batteries, Immersion cooling, Experimental dataset, Numerical simulation, Uncertainty quantification, Sensitivity analysis, Surrogate model, Bayesian calibration

1. Introduction

1.1. Industrial context

Encouraging the use of electric vehicles requires ultra-fast charging of batteries to close the gap between the time needed for filling the tank of a petrol car and charging an electric vehicle. The ultra-fast charging capability corresponds to high electric currents going through the Lithium-ion (Li-ion) cells. At the same time, race vehicles are turning to electrification requiring high average power out of large batteries: alternating sequences of high regenerative breaking (charging) and powerful accelerations (discharging). Those constraints provoke heat

*Corresponding author
Email address: elie.solai@inria.fr (Elie SOLAI)

loads on the battery pack, which forces derating of performances. Indeed, high temperatures cause damages to the battery pack and reduce the lifespan of the system.

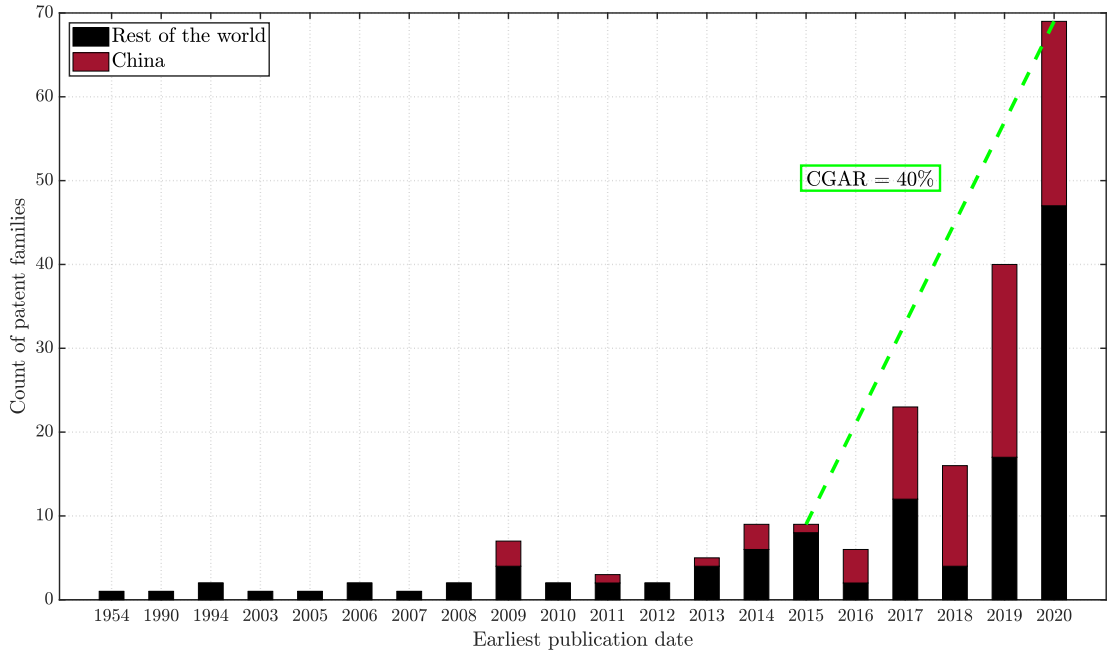

Figure 1: Rise of patents families related to liquid immersion cooling technology over the last 70 years, presenting a compound annual growth rate (CGAR) around 40%. Data extracted and plotted from the European Patent Office database by the company Capax Infinity.

Industrials focus their efforts on developing Battery Thermal Management Systems (BTMS) to keep the batteries in a safe range of temperatures during the vehicle operation and ensure temperature homogeneity between the cells and within a cell. Conventional indirect cooling techniques such as water cold plates can not cope with this high heat generation. A promising solution to reach high-performance cooling is immersion cooling technology [1, 2]. As it is highlighted in Fig. 1, immersion cooling recently received an increasing attention from BTMS manufacturers. The number of patents related to immersion cooling technology shows a significant rise since 2016. In such systems, a high heat transfer rate dielectric fluid flows in direct contact with the Li-ion batteries, and the liquid has access to a much wider cooling surface much closer to the hot spots.

1.2. Li-ion batteries immersion cooling experimental setup and dataset

Many experiments of immersion cooling configurations have been conducted in the literature. While experimental facilities and methods can differ, measurements are often related to the temperature evolution of Li-ion cells under various conditions. Notably, most references study the effect of charge and discharge rates on the batteries temperature evolution. These facilities usually feature a pack composed of few cells, going from a lonely cell as in [3] up to larger configurations as in [4] with 32 cells. The packs are immersed in fluid within a tank or enclosure. The fluid utilized is either air or coolants with better thermal performances. Cells temperatures are usually measured by thermocouples placed on the skin of the cells. Using

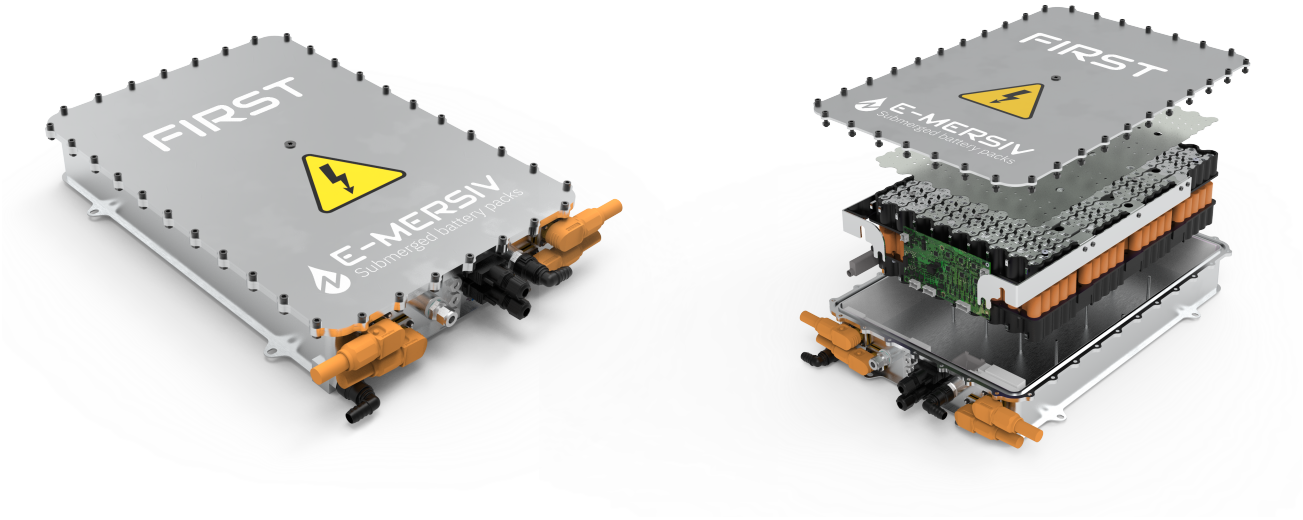

Figure 2: Battery module from the company e-Mersiv composed of 21700 cylindrical Li-ion cells - 5.2 [kWh]. Capable of 10 [C] for 10 [sec] and 7 [C] continuously, cooled by immersion in a dielectric fluid.

thermocouples on each of the cells allows evaluating the temperature uniformity within the packs. These setups focus on different parameters of interest, such as maximum temperature, maximum spatial temperature deviation and temperature uniformity, giving informative insights on the behavior and performances of immersion cooling systems. Let's review some results from the literature provided by such experimental investigations.

The immersion cooling experimental setups usually allow studying the impact of the geometry and the arrangement of the cells. Refs [5, 6, 4] studied the influence of arrangement geometries on the cooling effectiveness. Indeed, [4] showed experimentally that an aligned arrangement in straight rows of cells displays the best cooling capabilities, based on temperature measurements within the pack.

The thermal regimes cooling performances are also studied through those experimental setups. [7] assess the performances of a newly developed cooling system, a thermoelectric cooler, by comparing it against natural and forced convection cooling using the same facility. [8] also assess capabilities of their innovative oil impingement cooling technique. The reference [9] provides experimental measurements of temperature for the case of heated batteries immersed in a fluid, under different cooling regimes. The variety of fluids utilized allows to investigate the efficiency of air or liquid cooling involving more complex fluids. Also, for each fluid, several incoming velocities are applied and the resulting temperature evolution is measured.

Some authors use experimental setups to build or calibrate numerical models. For instance, [10] assess the heat generated by the batteries from temperature measurements and include it as a source term in the model to ensure good numerical reproducibility of the experimental data.

Many of the cited experiments use steady discharge rates in each investigated experimental condition. Only a few references perform temperature measurements while alternating charge, discharge, and rest cycles at different rates. In [3, 8] the temperature evolution the cells are investigated during such cycles.

The first contribution of the present paper is to describe an experiment, which gathers many of the features described above, providing novel experimental data. Precisely, the setup consists of a lab-scale battery pack of eight 18650 cylindrical cells immersed in a coolant and under a forced convection regime. The spacing between each cell and with the enclosure walls is narrow. In that sense, the current setup gets closer to realistic geometries of manufactured battery packs. Thermocouples measure temperatures at cathode and anodes locations for some of the eight cells. The experiment's goal is to measure the temperature evolution of the batteries submitted to different charging and discharging cycles. In addition, electrical characteristics such as voltage and electrical current are monitored and put in perspective with the temperature evolution. The several cycles investigated present various charging rates within the same experiment. The experimental measurements allow quantifying the effect of charging rates in a transient regime and how the cooling capabilities are affected by such variations. The experimental results are provided in a dataset available at [11].

1.3. Data-driven numerical model

The second contribution of this paper concerns the validation of a data-driven numerical model permitting to predict the performance of the BTMS system.

Several modeling approaches exist to perform the simulation of BTMS. The authors in [12] identify the modeling methods to represent the thermal and electrical behavior of the Li-ion batteries in immersion cooling systems. They state that the usual approach is either to consider the batteries and cooling system in either a 1D, 2D, 3D geometry or using a so-called lumped model.

The simulation of immersion cooling BTMS requires solving thermal and electrical equations to estimate the temperature, voltage and state of charge evolution of the Li-ion cells, under given discharging or charging conditions. For the thermal part, the classical approach is to use 2D or 3D computational fluid dynamics (CFD) models to solve the conjugate heat transfer in such configuration. Several references solve Navier-Stokes and energy conservation equations in various geometries of BTMS [13, 14, 15, 16, 10, 17]. CFD models allow predicting the temperature fields evolution in both solid (Li-ion batteries) and fluid (coolant) domains under different operation conditions of the BTMS. In terms of computational cost, solving the conjugate heat transfer for BTMS could turns out to be very costly if one seeks to represent the thousands of cells usually composing a real battery pack, as the one shown in Fig. 2.

Also, other types of models, involving some simplified approaches, can be found in literature to represent the thermal and electrical behavior of the batteries. For instance the authors in [18] developed a 1D electro-thermal model to couple the electrical parameters of the battery such as voltage and resistance, among others, with the temperature prediction of heated Li-ion batteries. The authors in [19] show a model representing the thermal and electrical performances of a battery and their interaction, using equivalent circuit models and electrical analogy to compute the heat generation in a simplified Li-ion cell. Also, the lumped body approach consider the temperature uniformly distributed in the battery. For example, [20] apply a lumped thermal model to compute the heat generation in the battery and heat transfer between the battery surface and surrounding fluid. The lumped and 1D model developed in these studies, featured a good representation of the temperature evolution with respect to experimental data.

Finally, some authors represent the whole physics, with higher fidelity, from the chemical level up to the heat transfer at the module level, mixing CFD models for the flow and

heat transfer with partial differential equations for the electro-chemical phenomenon. The references [21, 22] performed such a comprehensive approach.

A Battery Thermal Management System is a multi-physics system involving various uncertain parameters. First, thermal parameters, namely the radial and axial thermal conductivities, and the specific heat of the Li-ion cells involved in the energy equation are in practice really hard to evaluate due to the complex chemical structure of the Li-ion cells [23, 24, 25]. Furthermore, electrical parameters such as the internal resistance and state of health of the cell feature also complex behaviors. It is commonly agreed in the literature that the heat generated by the Li-ion cells is, for the most part, due to the Joule effect, coming from the internal resistance and the electric current going through the cells [26, 27]. Consequently, the internal resistance parameter is expected to significantly influence the temperature evolution of the Li-ion cells when solving the heat equation. Finally, parameters related to the fluid domain present as well some uncertainties. The mass flow rate of the cooling fluid is given indirectly by the operation of the pump generating the convective heat transfer. Due to the geometry of the arrangement of the Li-ion cells within the pack, it is hard to assert a value of the mass flow rate from the pump input instructions. Overall, uncertainties coming from those multi-physics parameters will generate considerable variability in the numerical model's temperature, voltage, and state of charge prediction. Most of the references addressing Uncertainty Quantification on Li-ion cells focus on the equations governing the electrochemical behavior within a Li-ion cell [28, 29, 30, 31]. Some authors [32, 33] focus on coupling electronics partial differential equations to the thermal equation to compute the heat produced within a single Li-ion cell. To the best of our knowledge, no references are studying the effects of uncertainties for the heat transfer between the batteries and a cooling fluid.

In this context, the second contribution of this paper is twofold, i) to develop a fast-to-evaluate model to reduce the computational constraints inherent to CFD models, ii) to illustrate the interest in a UQ-based approach to assess the model predictivity. Specifically, the heat transfer between the solid and fluid domains is solved by coupling the 2D heat equation in the solid domain with a heat balance in the fluid domain seen as a conduct. Electrical parameters are computed using equivalent circuit models and parameters' estimation through data tables related to specific Li-ion cells. Including uncertainties coming from the Li-ion batteries' thermal and electrical parameters permits assessing the impact of those multi-physical parameters uncertainties on the temperature predicted by the numerical model. In addition, experimental data are directly used to reduce these uncertainties and learn about the parameter values and the model behaviour thanks to the resolution of a Bayesian inverse problem. Finally, a sensitivity analysis is performed to get further insights into the behaviour of the whole system.

The article is structured as follows. First in section 2, the immersion cooling experimental setup is presented. The thermal performances of the system are quantified thanks to the results of this experiment. Then, Section 3 illustrates the numerical model and its performance on the experimental data reproducibility. Section 4 details the source of uncertainties related to the specified parameters. The mathematical framework to deal practically with the uncertainties is presented at this point. Finally, section 5 gives the results of the Bayesian calibration and uncertainty quantification approach in three different cases of discharging/charging conditions. Conclusions and perspectives outcoming of this study are drawn in section 6.

2. Experimental test case: lab-scale immersion cooling

The experimental case setup is represented in Fig. 3. It is made of a representative batch of eight cylindrical cells. The batteries used are the cylindrical cells 18650-VTC6 from Murata with 3 Ampere-hour capacity (denoted $[A \cdot h]$ in the following). They are stored in an enclosure, a cube with sides of 150 [mm]. The cells have a diameter of $d = 18$ [mm] and a height of $L = 65$ [mm]. They are spaced 0.5 [mm] from each other and staggered in a hollow shape that also lets a 0.5 [mm] spacing from the walls. A dielectric fluid loop circulates bottom-up in direct contact with the cells. The flow goes axially along with the cells within the enclosure, from the bottom to the top. The fluid is entering the enclosure at a speed of 0.04 $m.s^{-1}$. Temperature sensors are placed on the busbars, at the bottom and above sides of the cells. The position of the sensors in the battery pack is detailed in Fig. 3. The working fluid used in this experiment is the CFX70 from Chemours™ company. The physical properties of the fluid are detailed in Tab. 1.

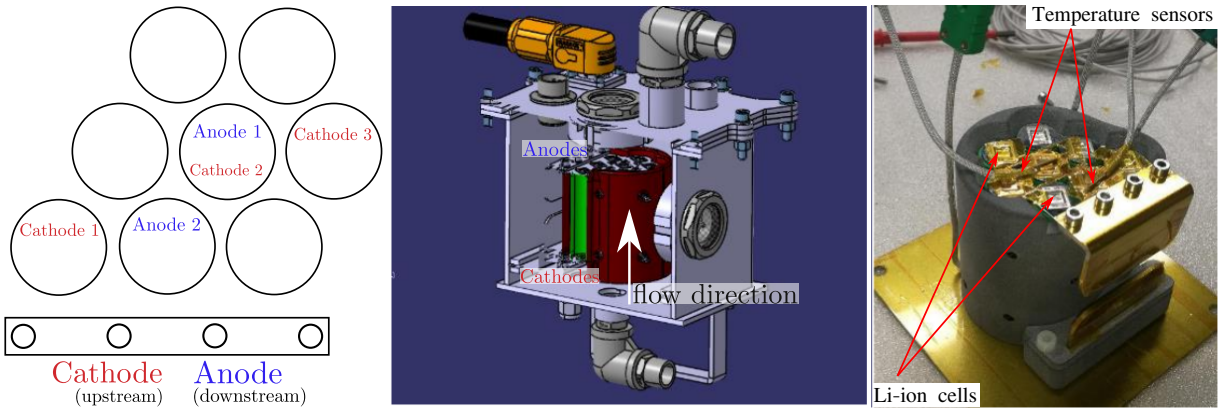

Figure 3: Experimental set up. Position of the temperature sensors (left), computer aided design (middle) and real set up (right).

Li-ion cells are submitted to different charging and discharging electric current cycles. The experimental cycles define the amplitude of the electric current inputted to the cells and the duration of charging and discharging sequences. In this study, two cycles conditions are applied: the first one named Datasheet cycle (DS) and the second Racing Cycle (RC). For one Li-ion cell, the DS cycle comprises a sequence of $I = -30$ [A] discharging current during 242 [sec] followed by a sequence of $I = 5$ [A] charging current during 1468 [sec]. The RC cycle comprises a alternation of 10 [sec] discharging at $I = -30$ [A] and 10 [sec] charging at $I = 30$ [A] sequences, during 672 [sec]. Then, a rest sequence with $I = 0$ [A] during 400 [sec] is applied. The nominal conditions of the experiment parameters are detailed in Tab. 2. The circulating fluid cools the heated batteries at a steady flow rate. The purpose of the experiment is to monitor the temperature evolution of the Li-ion cells using the temperature sensors shown in Fig. 3. The flow rate of the cooling fluid, the voltage and the electric current of the batteries are also monitored. This experimental setup allows investigating the effect of various input electric currents on the temperature behavior of the Li-ion cells, cooled by immersion at a steady flow rate.

The whole experimental data for both DS and RC cycles are available at the link provided in [11]. The dataset includes the measurements of the inlet, outlet fluid temperatures. Also, three cathodes temperatures at three different locations and two anodes temperatures at two

Property	Units	CFX70
Boiling point	^oC	70.6
Freeze point	^oC	< -80
Density at 25 ^oC	$g \cdot cm^{-3}$	1.63
Viscosity at 25 ^oC	cP	0.75
Heat of vaporization	$kJ \cdot kg^{-1}$	98
Liquid conductivity	$W \cdot (m \cdot K)^{-1}$	0.093
Liquid specific heat at 25 ^oC	$kJ \cdot (kg \cdot K)^{-1}$	0.75
Coefficient of expansion	K^{-1}	0.0014
Dielectric strength, 0.1" gap	kV	37
Volume resistivity	$\Omega \cdot cm$	$2.10 \cdot 10^{15}$
Dielectric constant		1.82
Ozone depletion potential (ODP)		0
Global warming potential (GWP)		< 20

Table 1: Physical properties of CFX70 fluid.

other locations within the pack are available. Finally, measurements of the voltage for one cell and the electric current going through the battery pack are provided. The provided measurements cover four cycles for the DS case and one cycle for the RC cycle.

	Mass flow rate $[L \cdot min^{-1}]$	Electrical current [A]	Sequences [sec]	Init. voltage [V]	Init. fluid temp $[^oC]$
Datasheet cycle (DS)	1.0	$I = -30$ $I = 5$	$t = [0; 242]$ $t = [242; 1468]$	4.16	45.22
Race cycle (RC)	1.0	$I = \pm 30$ in 10 [sec] periods 0	$t = [0; 672]$ $t = [672; 1045]$	3.58	45.28

Table 2: Nominal experimental conditions for DS and RC cycles.

The results of the experiment for the DS and RC cycles are shown in Fig. 4 and Fig. 5 respectively. Note that the electric current is measured for the whole pack of batteries. Thus, the values obtained in the plots for the electrical current are eight times higher than the values specified in Tab. 2 (given for one cell), according to the wiring of the pack.

For both cycles, the temperature discrepancy between the cathode and the anode temperatures is explained by their respective location in the enclosure. The cathode of Li-ion cells is at the entrance of the cooling fluid in the enclosure, while the anode is at the exit. As a consequence, the cooling fluid retrieves some heat while flowing around the cells. Also, from $t \approx 50$ [sec] in the RC cycle and the beginning of DS cycle, the fluid temperature at the inlet is lower than the temperature at the outlet, which agrees with the cooling process taking place within the enclosure. Overall, the flow rate measurements show that the steady condition is fulfilled, even if the rate presents some small noisy variations.

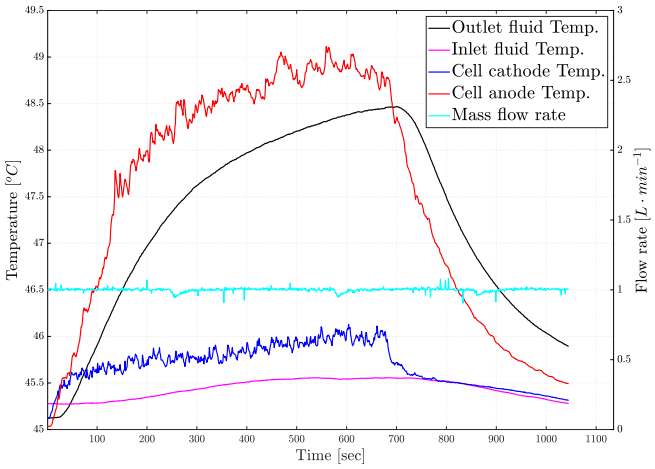

(a) Temperature and mass flow rate evolution

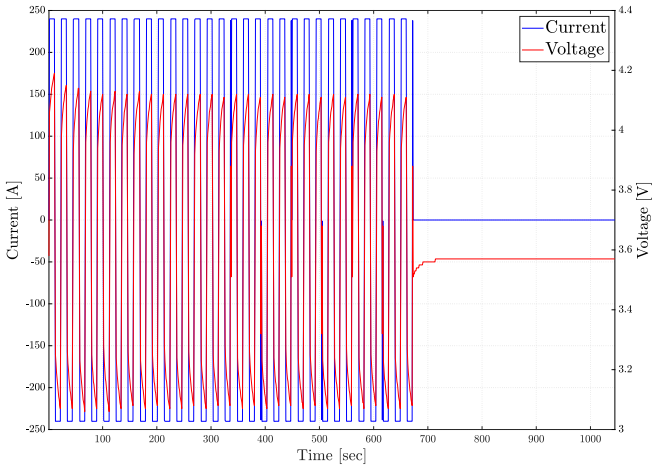

(b) Voltage and electric current evolution

Figure 4: Experimental measurements for the Race cycle.

For the RC cycle results in Fig. 4, heat is mostly produced during the alternation of charging and discharging sequences. Then, while the electric current is set to $I = 0$ [A], the fluid is cooling the batteries, decreasing the temperature as they are not producing heat anymore. For the anode, the temperature increases quickly during the first 400 seconds of the experiment. The slope of the temperature curve is significantly decreasing after $t = 500$ [sec]. The cathode temperature is increasing at a more regular rate during the charging/discharging sequence. Furthermore, the curve of the anode temperature shows a quick increase during the first 150 seconds of the experiment, which might appear to be uncorrelated with the following part of the curve. A plausible explanation can be drawn by considering that the internal resistance of a Li-ion battery can vary a lot at the beginning of its solicitation, notably because the stationary regime of chemicals reactions within the battery can be quite long to reach. During this period, the thermal behavior of the battery might not be as predictable as it would be on an established steady-state regime.

For the DS cycle results in Fig. 5, heating with a high discharging electric current at $I = -30$ [A] is much shorter than in the RC cycle. In contrast with the RC cycles results, a single heat transfer regime seems to be observable in this first sequence. Then, during the charging sequence at $I = 5$ [A], the heat produced by the battery is lower than the heat retrieved by the coolant. Moreover, temperature decreases, even if some electric current is still submitted to the batteries.

3. Numerical model

The model presented in this paper computes the transient heat transfer between a Li-ion battery and a surrounding fluid together with the evolution of electrical parameters, for the case of a Li-ion battery submitted to unsteady input electric currents. The approach chosen was to develop a model allowing insights on some parameters of interest evolution in immersion cooling configuration. For the thermal part, the variables computed by the model are the temperature of the Li-ion battery and surrounding fluid. The voltage and the state of charge of the battery are computed in the electrical part. The description of the whole

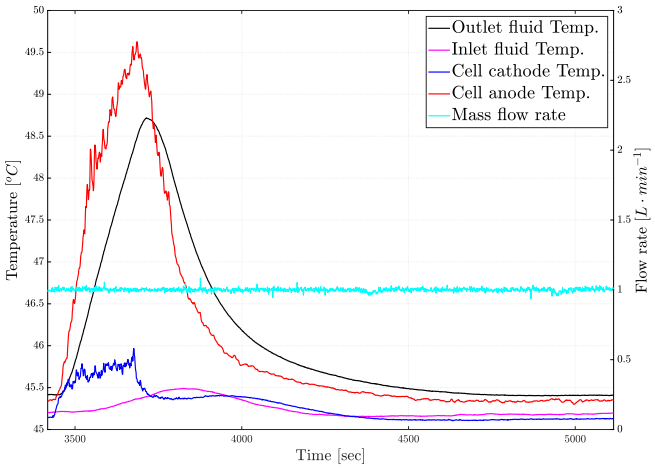

(a) Temperature and mass flow rate evolution

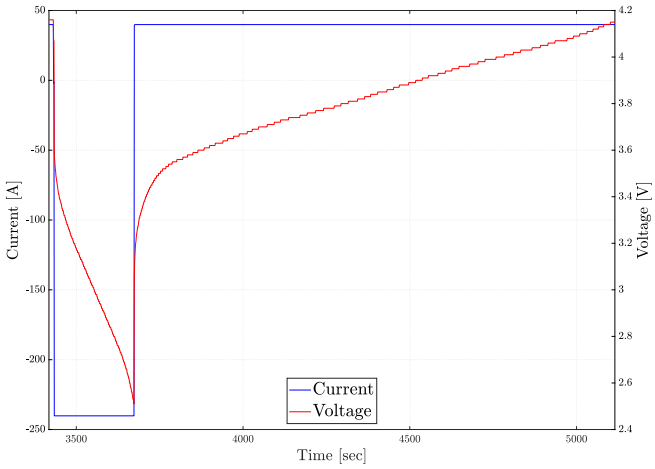

(b) Voltage and electric current evolution

Figure 5: Experimental measurements for the Datasheet cycle.

numerical model is resumed in Alg. 1.

3.1. Thermal equations

In this section, we describe the equations representing the heat transfer between the coolant (fluid domain) and the Li-ion cell (solid domain), both pictured in Fig. 7.

First, the solid domain Ω_s represents half of the cylindrical Li-ion battery in a 2D geometry. The temperature $T(\mathbf{x}_s, t)$, for a given position $\mathbf{x}_s \in \Omega_s$ and a time $t \in [t_0, t_f]$, is obtained by solving the heat equation:

$$\rho C_p \frac{\partial T(\mathbf{x}_s, t)}{\partial t} = \boldsymbol{\lambda} \Delta T(\mathbf{x}_s, t) + q \tag{1}$$

where ρ is the density of the Li-ion cell, C_p its specific heat capacity and $\boldsymbol{\lambda} = (\lambda_r, \lambda_z)$ is the vector of thermal conductivities in radial and axial directions respectively. q is the volumetric source term representing the heat generated within the Li-ion cell by the Joule effect and is computed as follows

$$q \propto R_0 \cdot I^2(t) \tag{2}$$

where R_0 stands for the internal resistance of the cell, and $I(t)$ is the electric current submitted to the batteries at a given time t. The heat is generated in the battery through the volumetric source term in Eq. 2 and then is spread in the domain through Eq. 1. As the computational domain represents only half of the Li-ion cell, a symmetry condition is applied for the temperature at the center of battery Γ_{sym}. For a position $\mathbf{x}_{\Gamma_{int}} \in \Gamma_{int}$, on the interface Γ_{int} between the fluid and solid domains, a Neumann condition is applied, giving the heat flux generated by the temperature difference between these domains:

$$\frac{\partial T(\mathbf{x}_{\Gamma_{int}}, t)}{\partial n} = -h_f S_{\Gamma_{int}} \Big(T(\mathbf{x}_f, t) - T(\mathbf{x}_s, t) \Big) \tag{3}$$

where $S_{\Gamma_{int}}$ is the surface of the whole boundary, $T(\mathbf{x}_f, t)$ the temperature in the fluid domain and $T(\mathbf{x}_s, t)$ the temperature in the solid domain at the other side of the interface. In practice,

the solid domain is meshed and finite differences scheme is used for space and time to solve the heat equation Eq. 1. The mesh containing 100 cells is visible in Fig. 6. It is meshed using a cartesian grid with the same number of cells in both radial and vertical direction. The mesh is then more refined in the radial direction.

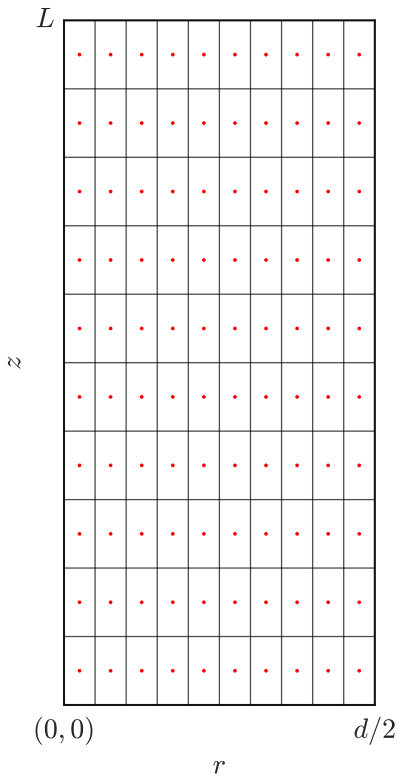

Figure 6: Mesh of solid domain with temperature unknowns in the center of each mesh cell

The energy transfer between the fluid and the solid domains is computed through the specific enthalpy of the fluid h. It is a function of the location in the fluid domain $\mathbf{x}_f$ and time t, so we denote the enthalpy $h(\mathbf{x}_f, t)$. The fluid layer around the battery is seen as a conduct. The heat balance for a control volume in the conduct is established, allowing to compute the specific enthalpy difference due to the heat produced by the Li-ion battery. Referring to Fig. 7, let's consider the control volume V in the fluid layer. The flow of the coolant is assumed steady, incompressible and the effects of gravity are neglected. Also, no mechanical power is brought to the fluid in this case. According to the first law of thermodynamics, for two locations of the fluid domain $\mathbf{x}_f$ and $\mathbf{x}'_f$ defining the control volume V in the conduct, the heat balance for any time t reads:

$$\dot{m}\left(h(\mathbf{x}'_f, t) - h(\mathbf{x}_f, t)\right) = \varphi_{th} \tag{4}$$

where $\dot{m}$ is the mass flow rate of the fluid flowing through the conduct. The heat flux φ_{th} defined in following represents the heat exchanged between the battery and the surrounding fluid in the control volume V:

$$\varphi_{th} = h_f \cdot S_V\Big(T(\mathbf{x}_f, t) - T(\mathbf{x}_s, t)\Big) \tag{5}$$

where h_f is heat transfer coefficient of the fluid. S_V is the surface of the interface between the solid domain and the control volume.

For a position $\mathbf{x}_{\Gamma_{inlet}}$ at the fluid inlet boundary Γ_{inlet}, a Dirichlet condition is applied for the specific enthalpy:

$$h(\mathbf{x}_{\Gamma_{inlet}}, t) = h_{ini}. \tag{6}$$

For a position $\mathbf{x}_{\Gamma_{outlet}}$ at the fluid outlet boundary Γ_{outlet}, an homogeneous Neumann condition is applied:

$$\frac{\partial h(\mathbf{x}_{\Gamma_{outlet}}, t)}{\partial n} = 0 \tag{7}$$

The temperature of the fluid is obtained by interpolation of tables linking the specific enthalpy, the pressure and the temperature using the REFPROP data base [34]. In the following, the interpolation operator of 2D gridded data for a scalar output quantity u is written as:

$$u = \mathcal{I}nterp_2(x_q, y_q, [\mathbf{T1}, \mathbf{T2}, \mathbf{TU}])$$

With this notation, the table $[\mathbf{T1}, \mathbf{T2}, \mathbf{TU}]$ contains the values of the quantity to compute $u \in \mathbf{TU}$, depending on the values in the vectors $\mathbf{T1}$ and $\mathbf{T2}$. The value u is computed for the query points $x_q \in \mathbf{T1}$ and $y_q \in \mathbf{T2}$, by interpolation on the values in $\mathbf{TU}$ corresponding to the query points. Numerically speaking, the $\mathcal{I}nterp_2$ function utilized is the Matlab 'interp2' routine (table lookup). The value u is obtained via a linear interpolation of the data available at the neighborhood of the query point (x_q, y_q).

The temperature of the fluid is then linked with the pressure P_0 and enthalpy $h(\mathbf{x}_f, t)$ in the table written $[\mathbf{h}, \mathbf{P}, \mathbf{Temp}]$, composed of possible values for enthalpy, pressure and temperature stored in the vectors $\mathbf{h}, \mathbf{P}, \mathbf{Temp}$ respectively. Then, temperature of the fluid at a location $\mathbf{x}_f$ and a time t is given as follows:

$$T(\mathbf{x}_f, t) = \mathcal{I}nterp_2\Big(h(\mathbf{x}_f, t), P_0;\ [\mathbf{h}, \mathbf{P}, \mathbf{Temp}]_{\text{REFPROP}}\Big) \tag{8}$$

Note that the query points for the 2D interpolation are the enthalpy $h(\mathbf{x}_f, t)$ and the pressure of the fluid P_0, which is known and assumed steady in this study. The pressure is set to $P_0 = 100$ [mBar]. The range of possible values in the temperature table $\mathbf{Temp}$ goes from -34.6^oC to $+120.5^oC$. The biggest discrepancy between two consecutive data is 0.67^oC.

The specific enthalpy h_{ini} at the inlet fluid boundary Γ_{inlet} is given by the following interpolation:

$$T_{ini} = \mathcal{I}nterp_2\Big(h_{ini}, P_0;\ [\mathbf{h}, \mathbf{P}, \mathbf{Temp}]_{\text{REFPROP}}\Big) \tag{9}$$

where T_{ini} is the temperature at the beginning of the simulation t_0 and also stands for the steady temperature outside the computational domains.

The equation system formed by Eq. 1, Eq. 4, Eq. 8 and the boundary conditions allows to compute the three unknowns of the problem: the temperature in the solid domain $T(\mathbf{x}_s, t)$, the specific enthalpy of the fluid $h(\mathbf{x}_f, t)$ and the temperature in the fluid domain $T(\mathbf{x}_f, t)$, at any time t.

As specified in the introduction, the objective of the uncertainty quantification approach is to compute statistics on some outputs of the numerical model. Specifically, in this paper, we focus on the mean of the temperature within the battery on the right side, nearby the

solid-fluid interface, as shown is Fig. 7. This zone is denoted Ω_{int}^{right} and its surface $S_{\Omega_{int}^{right}}$. This temperature is chosen to try to simulate the skin temperature of the battery as if it was located within a gap between two cells in a larger pack configuration. To get a scalar quantity, the mean of the temperatures in this area is computed, giving at any time t the temperature denoted $T_{qoi}(t)$. At any time t, the temperature of interest $T_{qoi}(t)$ is computed using

$$T_{qoi}(t) = \frac{1}{S_{\Omega_{int}^{right}}} \int_{\Omega_{int}^{right}} T(\mathbf{x}_s, t) d\mathbf{x}. \tag{10}$$

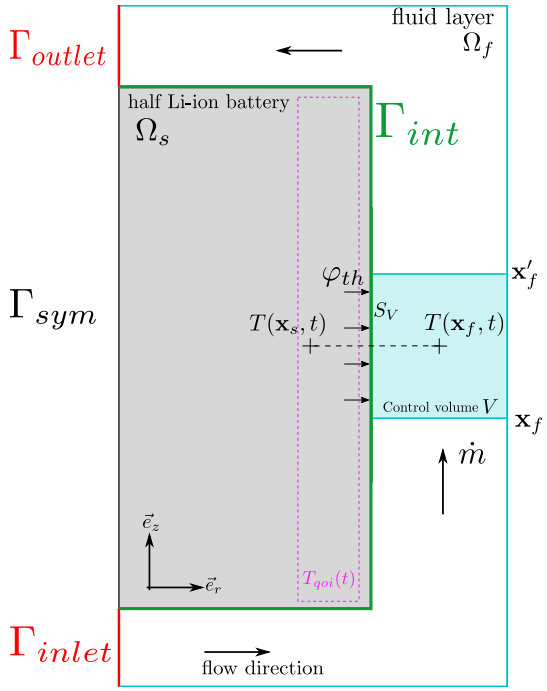

Figure 7: Computational domains: solid domain and fluid layer, control volume scheme for the specific enthalpy computation.

3.2. Electrical equations

Along with the thermal equations, electrical parameters of the Li-ion cells are also computed during the simulated time. In this study, the attention is focused on the computation of the voltage and state of charge evolution of the Li-ion battery.

The state of charge SOC of the cell is computed at each time t of the simulation using the relation:

$$SOC(t) = 1 \cdot SOH - \frac{I(t)}{C \cdot 3600} \cdot t \tag{11}$$

where C stands for the capacity of the cell in $[A \cdot h]$. SOH is the state of health of the battery, expressed with a percentage. $I(t)$ is the electrical current submitted to the battery at a time t. The capacity C is given at the beginning of the simulation by a 1D interpolation in tables linking the temperature and the capacity as follows

$$C = \mathcal{I}nterp_1\Big(T_{ini}; [\mathbf{Temp}, \mathbf{C}_{Ah}]\Big). \tag{12}$$

Similarly to the 2D interpolation function, $\mathcal{I}nterp_1$ is based on the 'interp1' function from Matlab. $\mathcal{I}nterp_1$ performs a 1D linear interpolation between data in the neighborhood of the query point, by comparison with $\mathcal{I}nterp2$ which takes two inputs x, y. The table $\mathbf{C}_{Ah}$ is a vector containing values of capacity from 2.88 to 3 $[A \cdot h]$ multiplied by the SOH parameter. The query point is the temperature at $t = 0$, knowing T_{ini}. The data in the table $\mathbf{C}_{Ah}$ are provided by the cell constructor Murata.

To compute the voltage of the battery, the Li-ion battery is approximated with an adapted Thevenin model [35]. It is represented in Fig. 8 with all the notations of the involved electrical parameters. A parallel RC circuit (with resistance R_1 and capacity C_1) is connected to the voltage source of the battery E_m and its internal resistance R_0. Following this approximation, the full voltage V of the battery, depending on time t, is given by the following relation:

$$V(t) = E_m(t) + Z(t) \cdot I(t). \tag{13}$$

The voltage source of the circuit is the electromotive force denoted E_m. Z is the impedance of the RC circuit representing the battery. E_m represents the no-load voltage of the open circuit. It is computed at each time t of the simulation using the following relation:

$$E_m(t) = E_i(t) - E_T(t). \tag{14}$$

Note that E_i is the voltage of a cell with no input electric current, and its value is obtained by interpolation of tables linking the electrical current, the state of charge and the voltage, as follows

$$E_i(t) = \mathcal{I}nterp_2\Big(I = 0, SOC(t); [\mathbf{I}, \mathbf{SOC}, \mathbf{E}_i]\Big). \tag{15}$$

Note also that E_T is the voltage of the cell dependant on the initial temperature and is obtained by interpolation of tables linking the temperature, the state of charge and the voltage, computed as follows

$$E_T(t) = \mathcal{I}nterp_2\Big(T_{ini}, SOC(t); [\mathbf{Temp}, \mathbf{SOC}, \mathbf{E}_T]\Big). \tag{16}$$

The table $\mathbf{E}_i$ and $\mathbf{E}_T$ contain values of the voltage with average discrepancy of 0.2 [V] between two consecutive data.

Following the RC circuits wiring in Fig. 8, the impedance Z of the battery is then expressed:

$$Z(t) = \frac{R_1(t)}{1 + R_1(t)C_1(t)} + R_0, \tag{17}$$

where R_1 and R_0 are the internal resistance of the RC circuit. R_0 represents the main contribution to the resistance of the battery. A constant value is chosen for this parameter. The resistance R_1 is obtained by interpolation of tables linking the temperature, the state of charge and the resistance:

$$R_1(t) = \mathcal{I}nterp_2\Big(T_{ini}, SOC(t); [\mathbf{Temp}, \mathbf{SOC}, \mathbf{R}_1]\Big) \tag{18}$$

The table $\mathbf{R}_1$ contains values of resistance from 0.5 to 10 $[m\Omega]$ with a maximum discrepancy of 4 $[m\Omega]$ between two values.

The query points are the initial temperature T_{ini} and the state of charge $SOC(t)$. Note that the capacity C_1 is the internal capacitance of the battery. It is interpolated from tables linking the temperature, the state of charge and the capacitance, computed as follows

$$C_1(t) = \mathcal{I}nterp_2\Big(T_{ini}, SOC(t); [\mathbf{Temp}, \mathbf{SOC}, \mathbf{C}_1]\Big) \tag{19}$$

The table $\mathbf{C}_1$ contains values of capacitance with a maximum discrepancy of $2.7 \cdot 10^{+3}$ Farads between two values.

Note that in practice, R_0 is assumed much bigger than R_1. To simplify the thermal model behavior and in the perspective of performing the calibration of the internal resistance parameter, the choice was made to consider only the contribution from R_0 for the internal resistance in the heat generation of the Li-ion battery in Eq. 1. All the data tables used in the previous equations are provided by the battery manufacturer.

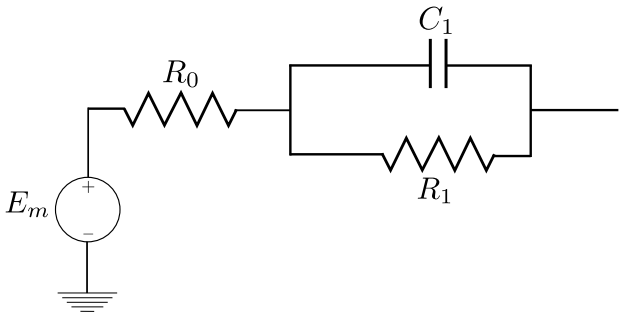

Figure 8: Adapted Thevenin equivalent model of the Li-ion battery.

In addition, this model allows to simulate the electrical parameters for an equivalent battery pack, rather than a single cell. To do that, the type of connections in the battery pack is considered, i.e. the parallel and serial configuration of the connections between all Li-ion cells. Using Kirchoff's laws, the equivalent input electrical current and voltage can be computed.

Algorithm 1 Numerical model

$t = 0$
  Init. thermal and flow parameters: $[\rho\ C_p\ \lambda_r\ \lambda_z\ \dot{m}\ h_f\ P_0]$
  Init electrical parameters: $[SOH\ C\ R_1\ C_1\ R_0]$
  Init. conditions:
    $T(\mathbf{x}_s, t = 0) = T(\mathbf{x}_f, 0) = T_{ini}$
    $h(\mathbf{x}_f, t = 0) = h_{ini}$
    $SOC(t = 0) = 1 \cdot SOH$
    $V(t = 0) = V_0$
while $t < t_f$ **do**
  Read electrical current input $I(t)$
  thermal model
    $q \leftarrow R_0 \cdot I^2(t)$
    Compute $T(\mathbf{x}_s, t)$ through Eq. 1. Apply the BC at $\Gamma_{int}, \Gamma_{sym}$
    Compute $h(\mathbf{x}_f, t)$ through Eq. 4. Apply the BC at Γ_{inlet}, Γ_{outlet}
    Compute $T(\mathbf{x}_f, t)$ through Eq. 8
    Compute the temperature of interest $T_{qoi}(t)$
  electrical model
    Compute $SOC(t)$ through Eq. 11
    Compute $E_m(t)$, $R_1(t)$, $C_1(t)$ through Eq. 14,15,16,18,19
    Compute $Z(t)$ through Eq. 17
    Compute $V(t)$ through Eq. 13
  $t \leftarrow t + \delta t$
end while

3.3. Numerical results

The thermal performances of the model are shown in Fig. 9 and Fig. 10. The temperature evolution computed by the numerical model is compared against the experimental data (Anode 1 temperature, see Fig. 3) and measurement error envelope. Same values of input parameters are taken for both cases so it is possible to compare quantitatively the performances of the model in each situation. The values of the thermal input parameters used in these simulations are given in Tab. 3. Those values were obtained after the calibration process detailed later in the study. Especially the range of values for the thermal conductivities and the specific heat capacity to initiate the calibration procedure were inspired from the references [24, 23].

Parameter	Symbol	Value	Units
Mass flow rate	$\dot{m}$	$2.925 \cdot 10^{-3}$	$kg \cdot s^{-1}$
Heat transfer coefficient	h_f	$2.140 \cdot 10^{+2}$	$W.m^{-2}.K^{-1}$
Internal resistance	R_0	$3.253 \cdot 10^{-3}$	Ω
State Of Health	SOH	$9.975 \cdot 10^{+1}$	%
Radial thermal conductivity	λ_r	$9.101 \cdot 10^{-1}$	$W.(mK)^{-1}$
Axial thermal conductivity	λ_z	$3.391 \cdot 10^{+1}$	$W.(mK)^{-1}$
Specific heat capacity	C_p	$1.157 \cdot 10^{+3}$	$J.(kg.K)^{-1}$

Table 3: Values of input thermal parameters.

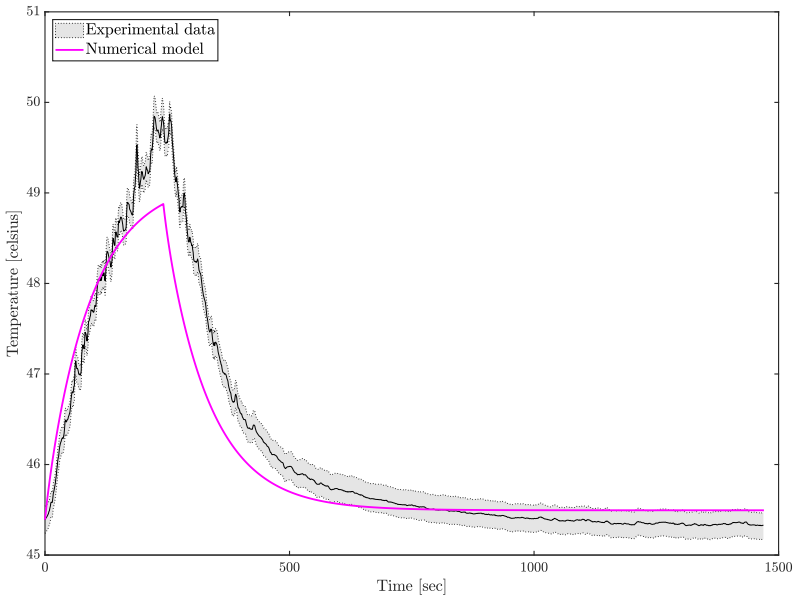

Figure 9: Temperature computed by the numerical model for the Datasheet cycle case.

For the Datasheet cycle in Fig. 9, the model seems to underestimate the battery temperature in the discharging sequence. However, the cooling period occurring during the charging

sequence seems well captured by the model and the final temperature is close to the experimental measurements. Several hypothesis could explain this temperature discrepancy during the discharging sequence. The temperature probes position in the experimental setup could induce an overheating which the model might not be able to compute. Indeed, the cells arrangement of the experimental setup generates variations in the coolant flow and overheating zones are expected to appear at some locations. It could be the case for the thermocouple position of Anode 1. The low order of the model for the fluid equations could limit its capability in reproducing such phenomenon. Also, the voltage of the battery drops rapidly in this sequence (see Fig. 5b). The low SOC at this point might provoke an higher heating rate from the cell and is omitted by the model.

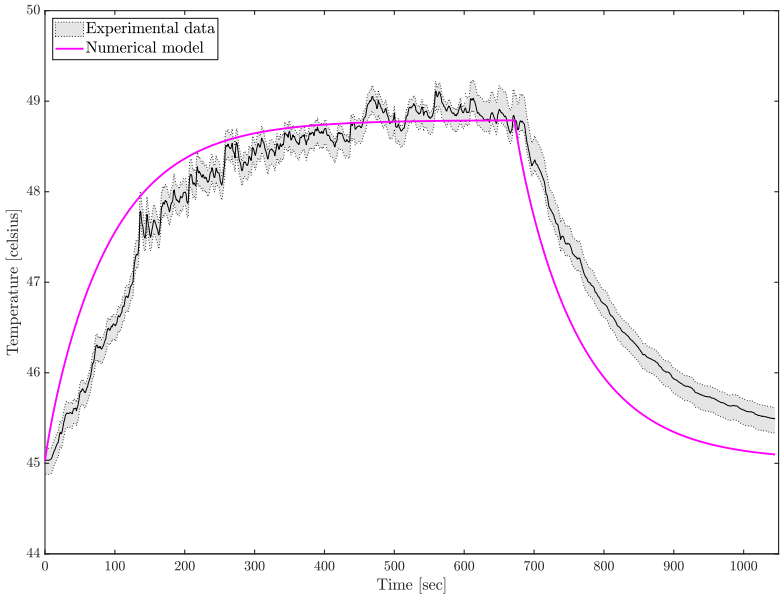

Figure 10: Temperature computed by the numerical model for the Race cycle case.

For the Race cycle in Fig. 10, the temperature predicted by the model gets close to the experimental data at the end of the heating sequence. The almost steady temperature regime, observable from the experimental measurements, seems also well represented by the model. From a physical perspective, in the Race cycle case, the experimental curve of temperatures in Fig. 10 shows a heating behavior in the first 150 seconds which seems not correlated to the shape of the curve after 200 seconds. A plausible explanation can be drawn by considering that the internal resistance of a Li-ion battery can vary a lot at the beginning of its solicitation, notably because the stationary regime of chemicals reactions within the battery can be quite long to reach. During this period, the thermal behavior of the battery might not be easy to be predicted by the model.

However, these numerical results show that the model reproduces well the overall heating and cooling behaviours of the immersed cells under different operating conditions.

4. Data-driven methodology

4.1. Source of uncertainties

As described in previous sections, solving the heat transfer in an immersion cooling configuration is a multi-physics problem involving physical parameters of different natures. Unfortunately, some of these parameters are hard to assess with good accuracy and confidence. Here, we propose an Uncertainty Quantification approach to address this problem. This section is devoted to characterize each uncertainty, i.e. consider a physically sound range of variation for each parameter and associate a prior distribution. Let's review which parameters are considered uncertain in this specific case of the Li-ion batteries immersive heat transfer problem.

First, the thermal parameters, $\lambda_r, \lambda_z, C_p$, are uncertain in the heat equation in the Li-ion cells, namely the thermal conductivities and the specific heat. The Li-ion cell is a "jelly-roll" layered structure of positive and negative electrodes, separator and electrolyte. A Li-ion battery is generally composed of a positive electrode made of lithium cobalt oxide, manganese oxide, or nickel oxide. The negative electrode is made of hard carbon or graphite. An electrolyte of a non-aqueous solvent is intercalated between the electrodes. This structure is responsible for the anisotropic thermal behavior of the batteries [36]. Due to the complex chemical structure of Li-ion cells and electrochemical reactions occurring between the "jelly-rolled" layers composing the cells, the radial and axial thermal conductivities and the specific heat capacity parameters are dependent on the electrochemical state of these layers [23, 24]. The highest fidelity models used to evaluate the axial and radial thermal conductivities of the batteries solve the electrochemical reactions within the layers of the cell, seen as porous media [24]. Even using this approach, it remains challenging to assess the thermal conductivity of all the layers in the structure.

Also, the heat generated by the Li-ion cells is mainly due to the Joule effect, coming from the electric current going through the cells and its inherent internal resistance [27, 10, 16, 26]. The above-described complex structure of a Li-ion cell is responsible for the obstruction of electrons transfer between the anode and cathode materials of the Li-ion cells. The behavior of the internal resistance parameter R_0 plays a crucial role in the heating process of the Li-ion cells. Then, to represent the heat transfer in a BTMS, it is essential to obtain an accurate model or value for the resistance parameter. The internal resistance depends mainly on the temperature of the Li-ion battery and its state of charge (SOC). In practice, it is costly to assess the effects of the temperature and the state of charge on the resistance, especially for an extensive range of temperatures. Most of the models include dependency either on temperature [26, 16, 10] or on both temperature and state of charge, but often for sparse values of these parameters [37, 38, 6]. Then it is practically difficult to assess a value for the internal resistance and its behavior in a wide range of temperatures with good accuracy.

The battery's state of charge quantifies using a unitless number the amount of electric current which the battery is still capable of delivering during a given time. It is computed from its nominal capacity expressed in $[A \cdot h]$ and the capacity at a given time during a charging or discharging sequence. The state of charge is a percentage of the state of health (SOH) of the battery, which is the actual value of its capacity when it is considered fully charged. The state of health is a way of quantifying the age of the battery. Many parameters could influence its values for a given battery, and various research efforts are focused on forecasting the evolution of this parameter [39, 40]. Considering the simulation of a battery

pack with numerous cells, it seems a reasonable approach to admitting a range of variation for the state of health, in percentages, to track its influence when modeling a BTMS.

Finally, the model used to represent the BTMS used in this case simulates the heat transfer between the Li-ion cell and the cooling fluid flowing around. The convective heat transfer performances between the solid and fluid domains, in this case, depends on the mass flow rate $\dot{m}$ and heat transfer coefficient of the fluid h_f. Those parameters are also hard to assess with reasonable accuracy in practice. The coolant used in this application is a complex fluid presenting excellent heat transfer performances. However, this fluid's heat transfer coefficient depends on temperature and pressure during operation and the flow speed used in the experiment, in a non-linear relationship. Besides, the value for the mass flow rate used during the operation of the BTMS is given indirectly through a pump generating the flow, which drives the forced convective heat transfer. Then, the value of the mass flow rate is never known precisely.

Overall, the seven following parameters are considered as uncertain: the mass flow rate $\dot{m}$, the heat transfer coefficient of the coolant h_f, the internal resistance R_0, the state of health of the cell SOH, the radial and axial thermal conductivities of the Li-ion cell λ_r,λ_z, the specific heat capacity C_p. Based on the user experience and the references mentioned above, the lower and upper bounds of the range of uncertainties for each parameter is given in Tab. 4.

$\mathbf{X}$	Parameter	Symbol	Lower bound X_i^{min}	Upper bound X_i^{max}	Units
X_1	Mass flow rate	$\dot{m}$	$2.64 \cdot 10^{-3}$	$3.96 \cdot 10^{-3}$	$kg \cdot s^{-1}$
X_2	Heat transfer coefficient	h_f	200	600	$W.m^{-2}.K^{-1}$
X_3	Internal resistance	R_0	$1 \cdot 10^{-3}$	$18 \cdot 10^{-3}$	Ω
X_4	State Of Health	SOH	98	102	%
X_5	Radial thermal conductivity	λ_r	0.77	1.55	$W.(mK)^{-1}$
X_6	Axial thermal conductivity	λ_z	10.37	45.83	$W.(mK)^{-1}$
X_7	Specific heat capacity	C_p	800	1200	$J.(kg.K)^{-1}$

Table 4: Uncertain parameters and bounds of their respective range of variation.

4.2. Uncertainty quantification problem definition

Let us define the mathematical framework allowing to deal with the uncertainties previously described. The uncertain inputs are stored in a vector $\mathbf{X} = [X_1, ..., X_7]$. To represent the uncertainties, each of the input parameter X_i is seen as a random variable, taking its values according to a given distribution denoted π_i, for $i = 1, ..., 7$.

The numerical model is from now seen as a black box function $\mathcal{M}$, giving the output from its evaluation at some input $\mathbf{X}$. Here, the purpose of the study is to estimate the temperature of the cell at given times of the simulation. The output of the computational model $\mathcal{M}$ is a vector of the temperatures of interest $T_{qoi}(t)$ evaluated at some times. Let us define the output vector of p elements as $\mathbf{T} = [T_1, ..., T_p]$ with T_i the temperatures at the times t_i, such that $T_i = T_{qoi}(t_i)$ for $i = 1, ..., p$. The numerical model evaluation on the input $\mathbf{X}$ results in the output vector $\mathbf{T}$ according to

$$\mathbf{T} = \mathcal{M}(\mathbf{X}). \tag{20}$$

One objective of Uncertainty Quantification aims at computing some statistics on the outputs of interest. In the current study, the attention is set on the first and second-order statistical moments of the output vector components, namely the mean and variance. For each component T_i of the vector of interest $\mathbf{T}$ those quantities are denoted as:

$$\begin{aligned} \text{Statistical mean:} \quad & \mathbb{E}[T_i] \\ \text{Statistical variance:} \quad & \mathbb{V}[T_i] \end{aligned} \tag{21}$$

Practically, the Monte Carlo method is used to compute those statistics on the outputs of interest. From a large number N_{MC} of input samples $\mathbf{X}^{(k)}$, $k \in [1, N_{MC}]$, the numerical model is evaluated through samples of the output:

$$\mathbf{T}^{(k)} = \mathcal{M}(\mathbf{X}^{(k)}) = [T_1^{(k)}, ..., T_p^{(k)}] \tag{22}$$

Then, the statistical mean and variance of each output T_i are evaluated using:

$$\begin{aligned} \mathbb{E}[T_i] &= \frac{1}{N_{MC}} \sum_{k=1}^{N_{MC}} T_i^{(k)} \\ \mathbb{V}[T_i] &= \frac{1}{N_{MC}} \sum_{k=1}^{N_{MC}} \left(T_i^{(k)} - \mathbb{E}[T_i] \right)^2 \end{aligned} \tag{23}$$

4.3. Surrogate model construction

To reach a proper convergence of these statistics, the number of samples N_{MC} should be high enough. The convergence requires then numerous evaluations of the computational model, which turns out to be very costly. The way around consists in building a mathematical function $\mathcal{M}^K$, mapping the output $\mathbf{T}$ with the input $\mathbf{X}$:

$$\begin{aligned} \mathcal{M}^K : \mathbb{R}^7 &\rightarrow \mathbb{R}^p \\ \mathbf{X} &\mapsto \mathbf{T} \end{aligned} \tag{24}$$

Here, we build this function is built using a stationary Gaussian Processes regression technique, known as Kriging [41, 42]. Its evaluation presents a very low computational cost compared to the numerical model.

First, we build a set of N_{LHS} points called the Design of Experiment (DOE). The Design of Experiment is obtained by sampling N_{LHS} vectors of inputs and by running the numerical model for each of these inputs. The DOE is the set of points denoted as

$$\mathcal{X}_{DOE} = \left\{ \left(\mathbf{X}^{(i)}, \mathbf{T}^{(i)} \right), \quad i = 1, ..., N_{LHS} \right\} \tag{25}$$

The set $\mathcal{X}_{DOE}$ contains several samples of the vectors of input $\mathbf{X}$ and output $\mathbf{T}$.

The Kriging model is dependent on so-called hyperparameters governing the form of the function. The construction of the Kriging model consists in finding the values of these hyperparameters maximizing the likelihood of the observations in $\mathcal{X}_{DOE}$. The computational cost of the Kriging construction is then reduced to solving the optimization problem to maximize the likelihood function.

To generate the Design of Experiment, the inputs points are sampled using the Latin Hypercube Sampling technique [43]. Here the DOE is made of $N_{LHS} = 170$ samples, chosen after a convergence study not reported here for brevity. This method allows to explore well the stochastic space for each input variable X_i with a reasonable number of samples. Each input variable X_i is sampled according to a uniform distribution $\pi[X_i]$, which range is given in Tab. 4:

$$X_i \sim \pi[X_i] = \mathcal{U}\left(X_i^{min}, X_i^{max}\right) \ , \ i = 1, ..., 7 \tag{26}$$

Finally to compute the statistics on the quantities of interest, Monte Carlo sampling is applied like in Eq. 23 using a number $N_{MC} = 4.2 \cdot 10^4$ of evaluations on the surrogate model $\mathcal{M}^K$ instead of the actual numerical model $\mathcal{M}$.

The accuracy of the surrogate model $\mathcal{M}^K$ with respect to the numerical model $\mathcal{M}$ is assessed by evaluating both models on an independent set of $N_{val} = 60$ input points. Values of both models are plotted against each other. As shown in Fig. 11, the values are close to the $y = x$ straight line for most of the input points. This results give good confidence on the ability of the surrogate model to represent the true numerical model.

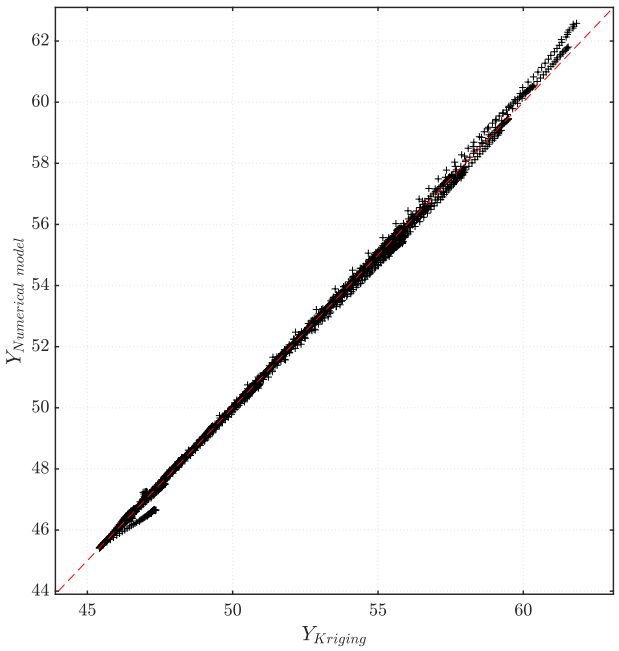

Figure 11: Plot of the values of temperatures computed by the surrogate model ($Y_{Kriging}$) against the values from the numerical model ($Y_{Numerical\ model}$), evaluated on an independent validation set of input points.

4.4. Prior and posterior uncertainties: Bayesian calibration of input parameters

One problem when doing Uncertainty Quantification is to formulate appropriate prior distributions of the input parameters, typically chosen based on the user's experience. The issue is to obtain more informative distributions for the input parameters, which give a model response close to the experimental data and with reduced variability in the output predictions.

The experimental measurements of temperatures $\mathbf{T}^{exp}$ can directly be used to learn more informative distributions of the inputs by solving a Bayesian Inverse problem [44]. Following the Bayes paradigm, the objective is to compute the distributions of the inputs by taking into account the information provided by the experimental data. It is called the posterior distribution and it can be computed using the Bayes theorem in Eq. 27:

$$\pi[\mathbf{X}|\mathbf{T}^{exp}] = \frac{\pi[\mathbf{T}^{exp}|\mathbf{X}] \cdot \pi[\mathbf{X}]}{\pi[\mathbf{T}^{exp}]} \tag{27}$$

$\pi[\mathbf{T}^{exp}|\mathbf{X}]$ stands for the likelihood and $\pi[\mathbf{X}]$ is the prior distribution defined in the previous section. $\pi[\mathbf{T}^{exp}]$ is seen as a normalization constant called the marginal likelihood.

The posterior distribution $\pi[\mathbf{X}|\mathbf{T}^{exp}]$ is approximated using a Markov Chain Monte Carlo (MCMC) algorithm [45, 46]. Using the Adaptive Metropolis algorithm [47], the Markov Chain is constructed by sampling iteratively candidate values for the inputs $\mathbf{X}^{(l)}$. The chain goes from the iteration (l) to $(l+1)$ by accepting a new candidate $\mathbf{X}^{(l+1)}$ with a probability of acceptance p_l, defined in the Adaptive Metropolis algorithm. This next sample is evaluated through the surrogate model $\mathcal{M}^K$ and accepted with the probability p_l.

4.5. Global sensitivity analysis

The global sensitivity analysis aims to quantify the effect of each uncertain input and their correlated effect on a given scalar quantity of interest [48]. The analysis is performed using a variance-based decomposition of the black box model known as Analysis of Variance (ANOVA) decomposition [49]. For notations purposes in this section only, let us denote $\mathcal{M}^Y$ a single scalar output of the lastly described numerical model, by comparison with $\mathcal{M}$ which outputs a vector of quantities of interest. The ANOVA decomposition of the model $\mathcal{M}^Y$ can be written as follows:

$$\mathcal{M}^Y(X) \overset{\text{ANOVA}}{:=} \underbrace{\mathcal{M}_0^Y}_{mean} + \underbrace{\sum_{i=1}^{7} \mathcal{M}_i^Y(X_i)}_{first\ order} + \underbrace{\sum_{i_1=1}^{7} \sum_{i_2=i_1+1}^{7} \mathcal{M}_{i_1 i_2}^Y(X_{i_1}, X_{i_2})}_{second\ order} + \cdots + \underbrace{\mathcal{M}_{1,\ldots,7}^Y(X_1, \ldots, X_7)}_{seventh\ order}. \tag{28}$$

The numerical model is seen as a sum of functions representing the contribution from each input variable X_i and their correlations up to the seventh order. This decomposition leads naturally to the definition of the normalized Sobol indices [50]. The first order Sobol index S_i^1 for an input variable X_i is defined by:

$$S_i^1 = \frac{\mathbb{V}\left[\mathbb{E}[\mathcal{M}^Y(X)|X_i]\right]}{\mathbb{V}\left[\mathbb{E}[\mathcal{M}^Y(X)]\right]} \tag{29}$$

The first order index quantifies the effect of the variable X_i only on the variability of the quantity of interest Y by computing the variance ratio in Eq. 29. The total Sobol index S_i^T for the variable X_i is computed as follows

$$S_i^T = 1 - \frac{\mathbb{V}\left[\mathbb{E}[\mathcal{M}^Y(X)|\bar{X}_{\setminus i}]\right]}{\mathbb{V}\left[\mathbb{E}[\mathcal{M}^Y(X)]\right]} \tag{30}$$

where $\bar{X}_{\setminus i}$ represents the set of all input variables and their combinations except X_i. The total Sobol index quantifies the impact of the variable X_i and its correlation with all other

variables on the variability of Y. For a given input X_i, a Sobol index close to 1 means that this variable has a great impact on the variability of the quantity of interest Y. On the opposite, a Sobol index close to 0 means that the quantity Y is almost independent on the variability of X_i. Note that for a given quantity of interest, all the Sobol indices should sum to 1. In practice, the input variables are sampled according to a given distributions and the Sobol indices are computed using Monte Carlo evaluations of the specified quantities in Eq. 29 and in Eq. 30.

5. Results

5.1. Posterior distributions calibrated from the Datasheet cycle case. Forward propagation of the posterior distributions.

The Bayesian inverse problem is solved using the Datasheet cycle case which the input current cycle is described in section 2. In this section, the simulation is performed only on the first 250 seconds of the cycle during the discharging sequence. The experimental data $\mathbf{T}^{exp}$ selected to learn the distributions is constituted of six measurements of temperatures at different times expressed in seconds and stored in the following vector: $t^{exp} = [49\ 99\ 129\ 159\ 199\ 239]$. For computational reasons related to the performances of MCMC algorithm, the choice have been made to compute the posterior distributions with only six measurements of the discharging sequence. In Fig. 12 are shown the posterior distributions of the seven uncertain inputs parameters obtained after running the MCMC algorithm. The units for each of the parameters are given in Tab. 4. The first consideration from these results is that the supports of the posterior probability density functions (PDF) are significantly more narrow than the prior uncertainties arbitrarily defined in section 4. The MCMC simulation allowed us to detect which values of the inputs are more likely to give a numerical response close to the experimental data, i.e. the values close to the peak of each distribution.

Because of narrower shapes of inputs' distributions, the variance of predicted temperatures is expected to be reduced. In Fig. 13, distributions of the temperatures computed by the surrogate model are shown, using the prior (blue) and posterior (red) distributions as inputs. The uncertainty in the predicted temperature is significantly decreased. When sampling the surrogate model from the posterior distributions, the values of the inputs $\mathbf{X}$ are more likely to be closer to each other compared to a sampling from the broad prior distributions. This fact might be an interpretation to explain why the model's response comprises a narrow range of values.

In addition, one can note that the distributions of the posterior predictions embrace well the experimental data and its measurement error envelopes. Then, an outcome of the MCMC simulation stands as a validation of the ability of the numerical model to reproduce the experimental data through its accurate representation with the surrogate model.

The approach can be extended to more than six quantities of interest, i.e. to many output temperatures at times covering the whole discharging sequence. In a similar way to section 4.3, a surrogate model is constructed mapping the inputs $\mathbf{X} \in \mathbb{R}^7$ to a vector of 49 temperatures of interest $\mathbf{T} = [T_1, ..., T_{49}]$. The mean and variance of each temperature of interest are computed using Eq. 23 and using the surrogate model. These statistics are computed by sampling the surrogate model from the prior and posterior distributions of the inputs. The comparison's results between the prior and posterior sampling are shown in Fig. 14. The blue and red crosses represent the mean of the estimated temperature of interest

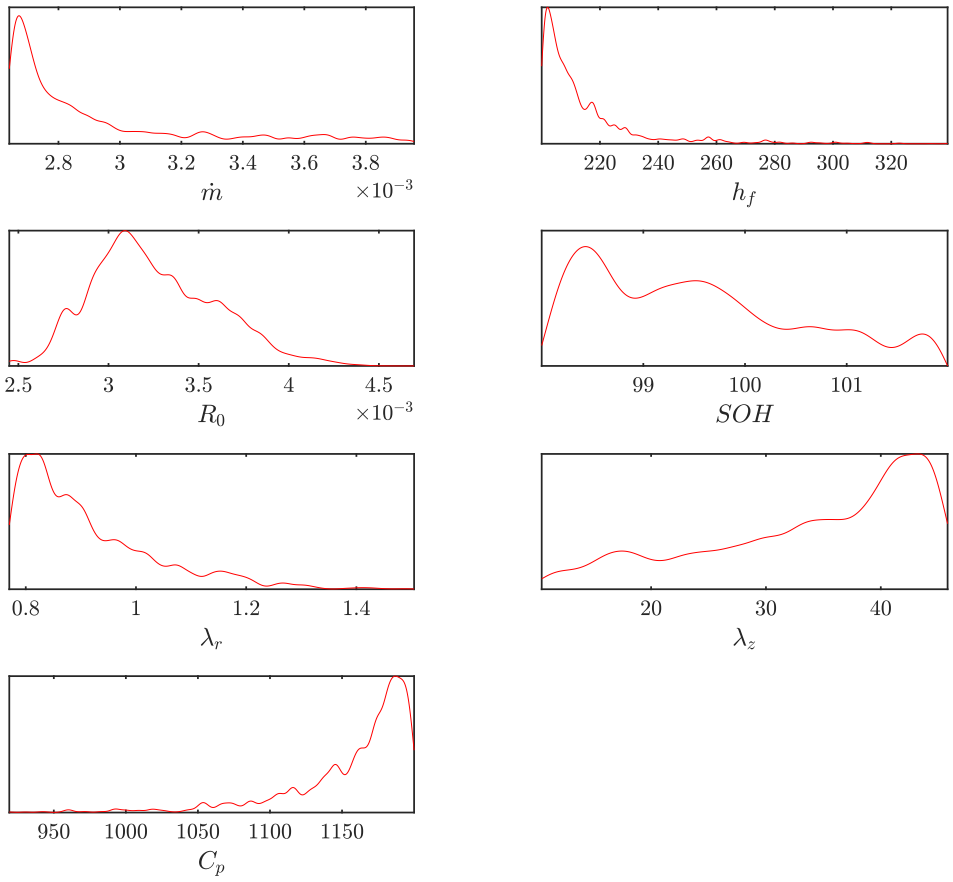

Figure 12: Posterior distributions of the input parameters after the calibration.

with the prior and posterior distributions, respectively. The blue and red areas represent the 95% confidence interval, computed with prior and posterior distributions, respectively.

This plot of the statistics on the whole simulation cycle sampled from the posterior and prior distribution strengthen the results from Fig. 13. The uncertainty reduction in the numerical prediction is highlighted by the comparison of the standard deviation envelopes. The standard deviation and mean sampled from the posteriors compare well to the experimental measurements, which gives reasonable confidence in the ability of the numerical model to reproduce the experimental temperature measurements.

5.2. Application: Propagation of the calibrated distributions on the experimental Race Cycle case

Distributions calibrated from the experimental Datasheet cycle can be used to reproduce another experimental cycle, the Race cycle. The cycle reproduced here consists of the discharging sequence of 672 [sec] and the rest sequence with no electric current of 400 [sec]. The surrogate model is constructed from a set of numerical simulations representing these

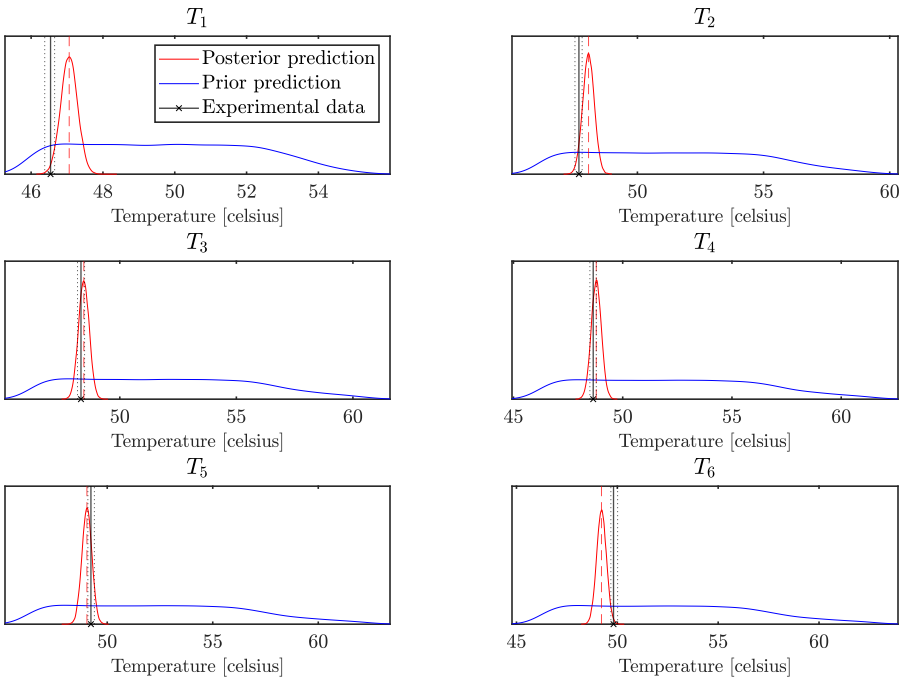

Figure 13: Distributions of the prior and posterior predictions for the six quantities of interest. Comparison with experimental measurements and error envelopes.

experimental conditions. In the present case, the surrogate model outputs 53 temperatures of interest covering the full simulated time of 1072 [sec]. The posterior distributions calibrated from the DS experimental conditions, obtained in 5.1, are directly used to sample the inputs and estimate the mean and variance of each temperature of interest through the surrogate model evaluations. The results are shown in Fig. 15.

The plot of the mean values and standard deviation envelopes are close to the experimental measurements. These results show that the values and the distributions of the inputs learned from the Datasheet cycle are reproducible with other conditions. This trend ensures further confidence in the numerical model behavior and the learned values of the inputs.

5.3. Application: forward propagation of calibrated distributions on a realistic race cycle and sensitivity analysis

This section aims to use distributions and associated probabilities for the input parameters from the previously described experimental conditions in a pure design perspective. Here, input conditions for the electric current simulate an actual race cycle, composed of numerous alternating charge and discharge sequences. These sequences aim at representing a real usage of the vehicle submitted to racing conditions. The simulated time is 1115 [sec]. The discharging sequences stand for the short and numerous accelerations of the car. The charging sequences represent the regenerative braking that loads the battery pack when the car slows down. The electrical part of the numerical model is adapted to represent the voltage and state of charge of a full battery pack composed of thousands of Li-ion batteries. The equations used are Eq. 13 and Eq. 11. The cells' connections within the battery pack allow computing

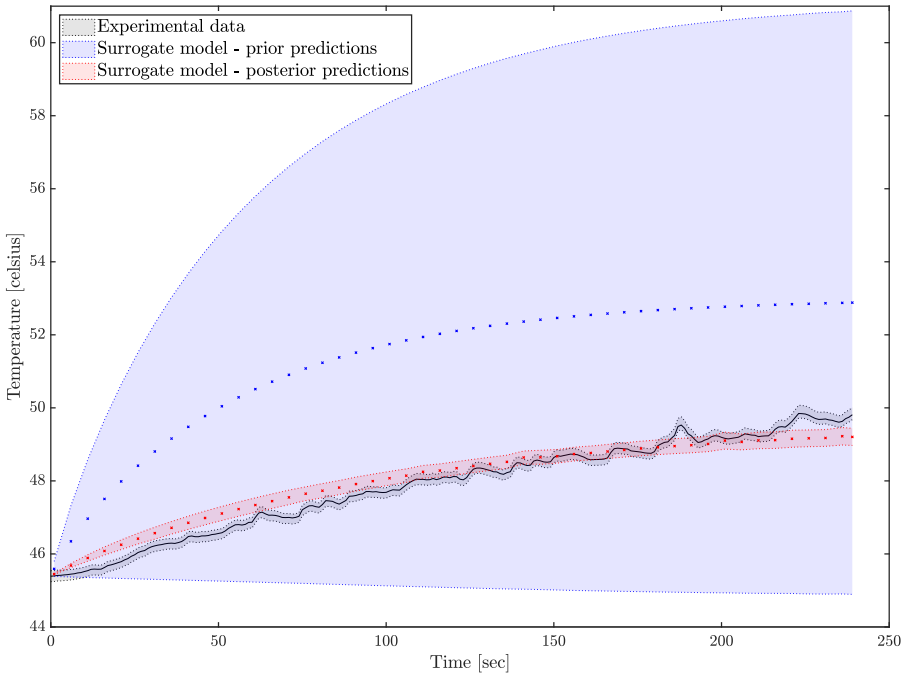

Figure 14: Posterior and prior predictions of the surrogate model mean and 95% confidence interval. Comparison with experimental measurements and error envelope.

the equivalent voltage and electric current, using Kirchoff's laws. For the thermal part, the heat transfer is still computed for an equivalent single-cell Li-ion representing the battery pack as described in section 3.

A surrogate model is built to map the inputs $\mathbf{X}$ to 56 temperatures of interest covering the simulated time. We use the same procedure as in sections 5.1 and 5.2. Then, inputs are sampled according to the calibrated distributions, and Monte Carlo evaluations give the mean and variance of the temperatures of interest. Fig. 16 shows the mean and standard deviation envelopes of the surrogate model temperature predictions by sampling from the prior (blue) and posterior (red) distributions. As in Fig. 14, the sampling from the posterior shows a significant variance reduction in the model predictions. The calibration process is then essential when designing the system, as the temperature interval of 95% confidence is much narrower than sampling from the priors.

Besides, the mean for each of the temperatures of interest presents periodic and local slopes switch, while having a global rising trend. This trend results from the high-frequency alternation of charging and discharging sequences, while the temperature of the Li-ion cell is slightly rising during the simulation.

To get further analysis elements on the BTMS' behavior under these real racing conditions, a global sensitivity analysis is performed by computing the Sobol' indices. In this section, we focus on both the electrical and thermal behaviors of the system. Hence, the quantities of interest are the minimal value of the state of charge SOC, the minimal value of voltage V and the maximal value of temperature T_{qoi} reached during the simulated time

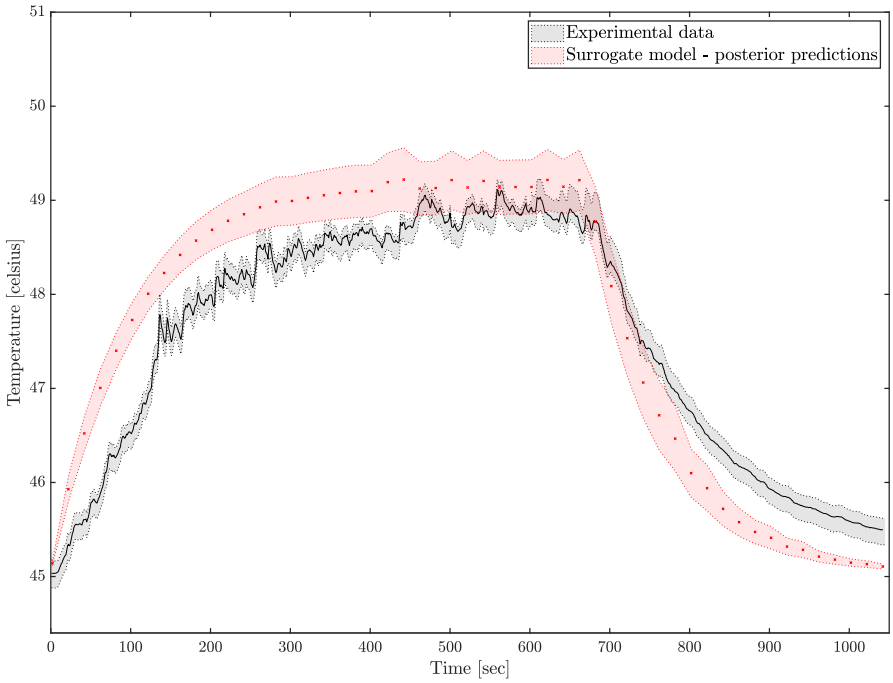

Figure 15: Posterior predictions in the Race Cycle case. Comparison with experimental measurements.

from t_0 to t_f. These quantities are denoted:

$$\begin{aligned} Y_1 &= \min_{t\in[t_0,t_f]} SOC(t) \\ Y_2 &= \min_{t\in[t_0,t_f]} V(t) \\ Y_3 &= \max_{t\in[t_0,t_f]} T_{qoi}(t) \end{aligned} \tag{31}$$

Practically, an other surrogate model is constructed to map the inputs $\mathbf{X}$ to the three scalar quantities of interest. The total Sobol' indices and first order Sobol' indices for each quantity of interest are shown in Fig. 17 and in Fig. 18 respectively and detailed in Tab. 5 and Tab. 6.

	$\dot{m}$	h_f	R_0	SOH	λ_r	λ_z	C_p
Y_1	0.0000	0.0000	0.0098	0.9879	0.0000	0.0000	0.0000
Y_2	0.0000	0.0000	0.1360	0.8581	0.0000	0.0000	0.0000
Y_3	0.1955	0.1668	0.5937	0.0148	0.0029	0.0220	0.0002

Table 5: Total Sobol' indices for the three quantities of interest.

The total and first-order Sobol' indices underly the same conclusions about the model's behavior. There is no significant difference between the results from the total and first-order

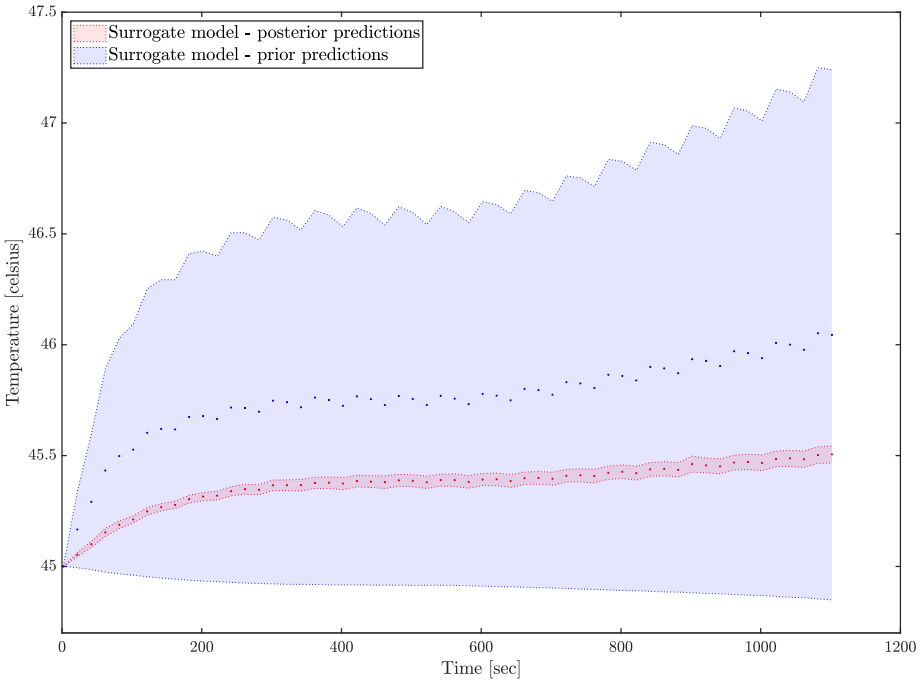

Figure 16: Posterior and prior predictions of the surrogate model mean and 95% confidence interval, for the real racing case.

	$\dot{m}$	h_f	R_0	SOH	λ_r	λ_z	C_p
Y_1	0.0021	0.0021	0.0114	0.9901	0.0021	0.0021	0.0021
Y_2	0.0046	0.0046	0.1383	0.8636	0.0046	0.0046	0.0046
Y_3	0.2053	0.1748	0.5978	0.0236	0.0123	0.0313	0.0096

Table 6: First order Sobol' indices for the three quantities of interest.

indices for all three quantities of interest. Then, input parameters do not feature a strong correlation effect between each other.

About the minimum of SOC, the parameter showing the most significant impact on its variability is the battery's state of health with a total and first-order Sobol index value close to one. For the minimum voltage, the state of health has the most significant influence on its variability. The battery's internal resistance has a non-negligible impact as well, with Sobol' indices around 0.13. Physically, the state of charge of the Li-ion cell is directly related to its voltage, so it was expected to see the SOH having the most considerable influence on this parameter. In the same way, the internal resistance is also physically directly related to the voltage. However, the Sobol analysis shows that the impact of the resistance is smaller than the state of health on the voltage variability.

Finally, regarding the maximum temperature computed during the simulations, the thermal parameters influence different magnitudes. The first lesson is that the internal resistance

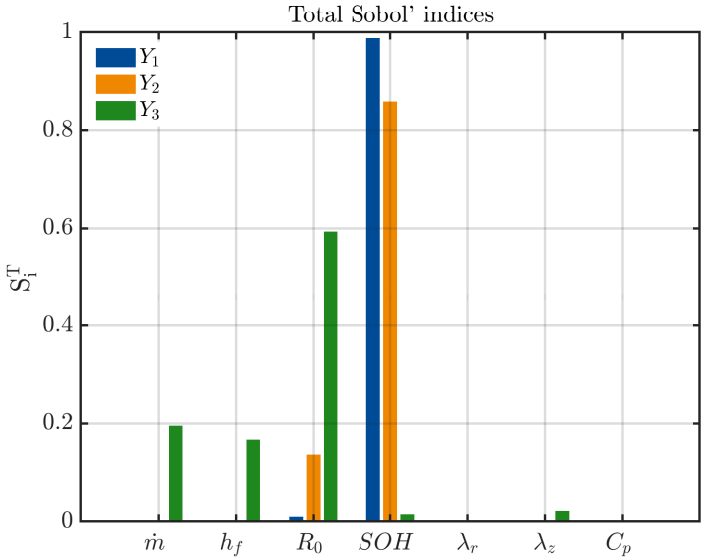

Figure 17: Total Sobol' indices for the three quantities of interest.

presents the most significant impact on the variability of the maximal temperature. Another consideration from first-order Sobol' indices in Fig. 18 is that the parameters related to the convective heat transfer, namely the mass flow rate $\dot{m}$ and the heat transfer coefficient of the fluid h_f have indices around 0.2. The impact of these parameters is considerably more important than the parameters playing a role in the heat equation within the battery, namely λ_r, λ_z and C_p. In conclusion, through the internal resistance R_0, the Joule effect seems to be the critical element governing the thermal behavior of the battery.

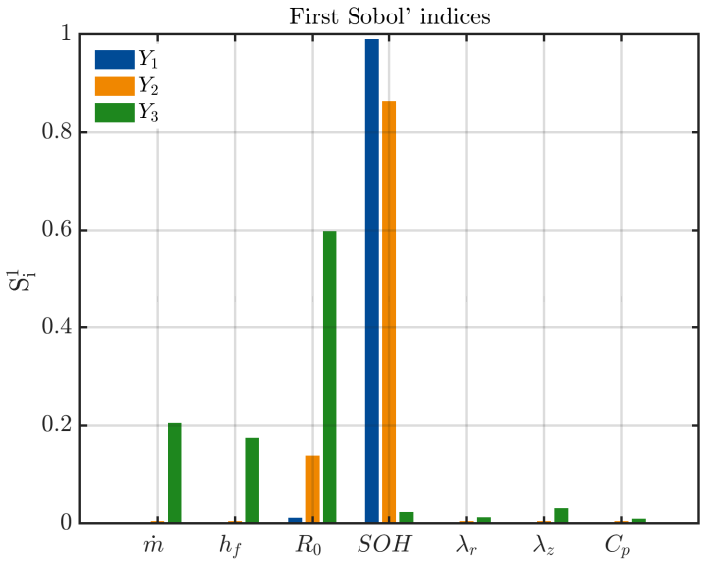

Figure 18: First order Sobol' indices for the three quantities of interest.

6. Conclusion

In this study, we propose a data-driven fast numerical model to simulate the Immersion Cooling of a Lithium-ion Battery Pack. First, we illustrate an experimental setup representing a small battery pack immersed in a cooling fluid, that was used to measure the batteries' temperatures under different charging and discharging cycles conditions. The results of the experiment allowed us to quantify the cooling performances of the immersive system. In addition, the experiment allows to evaluate the effect of electrical current rates on the thermal behavior of the Li-ion batteries.

Secondly, a simulation under uncertainties of the immersion cooling system was performed in this work. A numerical model was developed to simulate the heat transfer between a Li-ion battery and a coolant. Then, uncertainties coming from multi-physical parameters involved in the immersive heat transfer were considered. Uncertainty quantification methods, such as Kriging surrogate models and Monte Carlo evaluations, allowed treating the uncertainties coming from the model's physical parameters. The experimental data were used directly to compute posterior distributions of the input parameters by solving the Bayesian inversion problem. Posterior learned distributions allowed reducing significantly the uncertainty in the model prediction of temperatures. The model and calibrated distributions showed good reproducibility capability when comparing the numerical results to the experimental data under different conditions. Specifically, the support of the posterior distributions is significantly reduced with respect to the prior. The propagation of the posterior distributions showed a good ability to match the experimental data, with a very narrow 95% confidence interval in both Datasheet and Race cycles. Finally, the posterior distributions and the numerical model were used to assess the temperature response of a BTMS under realistic racing conditions.

The Sobol sensitivity analysis showed the role of each uncertain input in the variability of the several quantities of interest considered. First, the total and first order Sobol indices showed very similar values, for the three quantities of interest. Then the uncertain parameters considered don't show a strong dependency between each other in the variability of the outputs. Also, the sensitivity analysis showed that the SOH is the most influential parameter for the variability of the minimum voltage and SOC with values around 0.9 and 0.8 respectively. For the maximum temperature, the internal resistance R_0 is the most important parameter with a total index close to 0.6. The mass flow rate and heat transfer coefficient show a significant influence too with total indices around 0.2.

This global sensitivity analysis allows to draw conclusions related to the simulation of a Battery Thermal Management System. For the thermal part, it is crucial to have an accurate model to represent internal resistance because of its impact on the battery temperature evolution. Also, representing the conjugate heat transfer by developing 2D or 3D CFD models for the fluid domain could provide more information about assessing the value of the heat transfer coefficient and guess more precisely the effect of the mass flow rate. Finally, for the electrical parameters, the state of health parameter should be simulated with good accuracy to correctly represent the effects induced by the ageing of the batteries. As shown in some references [38, 51], the SOC of the battery depends strongly on its SOH and have an impact on the internal resistance parameter. Developing enhanced models for these parameters should allow to represent the thermal and electrical behavior of Li-ion batteries with higher fidelity.

Acknowledgment

This work was supported by Inria and Exoes, co-funded by Inria Bordeaux Sud–Ouest and the Conseil Régional de la Nouvelle Aquitaine under Grant Agreement No 2016-1R60205-00007444-THESE.

Numerical experiments presented in this paper were carried out using the PlaFRIM experimental testbed, supported by Inria, CNRS (LABRI and IMB), Université de Bordeaux, Bordeaux INP and Conseil Régional d'Aquitaine (see https://www.plafrim.fr/).

References

[1] X. Zhang, Z. Li, L. Luo, Y. Fan, Z. Du, A review on thermal management of lithium-ion batteries for electric vehicles, Energy 238 (2022) 121652. doi:10.1016/j.energy.2021.121652.
URL https://linkinghub.elsevier.com/retrieve/pii/S0360544221019009

[2] Q. Wang, B. Jiang, B. Li, Y. Yan, A critical review of thermal management models and solutions of lithium-ion batteries for the development of pure electric vehicles, Renewable and Sustainable Energy Reviews 64 (2016) 106–128. doi:10.1016/j.rser.2016.05.033.
URL http://linkinghub.elsevier.com/retrieve/pii/S1364032116301435

[3] D. W. Sundin, S. Sponholtz, Thermal Management of Li-Ion Batteries With Single-Phase Liquid Immersion Cooling, IEEE Open Journal of Vehicular Technology 1 (2020) 82–92. doi:10.1109/OJVT.2020.2972541.
URL https://ieeexplore.ieee.org/document/8988178/

[4] Y. Fan, Y. Bao, C. Ling, Y. Chu, X. Tan, S. Yang, Experimental study on the thermal management performance of air cooling for high energy density cylindrical lithium-ion batteries, Applied Thermal Engineering 155 (2019) 96–109. doi:10.1016/j.applthermaleng.2019.03.157.
URL https://linkinghub.elsevier.com/retrieve/pii/S1359431118376695

[5] X. Tan, P. Lyu, Y. Fan, J. Rao, K. Ouyang, Numerical investigation of the direct liquid cooling of a fast-charging lithium-ion battery pack in hydrofluoroether, Applied Thermal Engineering 196 (2021) 117279. doi:10.1016/j.applthermaleng.2021.117279.
URL https://linkinghub.elsevier.com/retrieve/pii/S1359431121007158

[6] Z. Wang, X. Tong, K. Liu, C.-M. Shu, F. Jiang, Q. Luo, H. Wang, Calculation methods of heat produced by a lithium-ion battery under charging-discharging condition, Fire and Materials 43 (2) (2019) 219–226. doi:10.1002/fam.2690.
URL https://onlinelibrary.wiley.com/doi/abs/10.1002/fam.2690

[7] X. Li, Z. Zhong, J. Luo, Z. Wang, W. Yuan, G. Zhang, C. Yang, C. Yang, Experimental Investigation on a Thermoelectric Cooler for Thermal Management of a Lithium-Ion Battery Module, International Journal of Photoenergy 2019 (2019) 1–10. doi:10.1155/2019/3725364.
URL https://www.hindawi.com/journals/ijp/2019/3725364/

[8] A. Trimbake, C. P. Singh, S. Krishnan, Mineral Oil Immersion Cooling of Lithium-Ion Batteries: An Experimental Investigation, Journal of Electrochemical Energy Conversion and Storage 19 (2) (2022) 021007. doi:10.1115/1.4052094.
URL https://asmedigitalcollection.asme.org/electrochemical/article/19/2/021007/1115735/Mineral-Oil-Immersion-Cooling-of-Lithium-Ion

[9] C. Menale, F. D'Annibale, B. Mazzarotta, R. Bubbico, Thermal management of lithium-ion batteries: An experimental investigation, Energy 182 (2019) 57–71. doi:10.1016/j.energy.2019.06.017.
URL https://linkinghub.elsevier.com/retrieve/pii/S0360544219311405

[10] F. He, X. Li, L. Ma, Combined experimental and numerical study of thermal management of battery module consisting of multiple Li-ion cells, International Journal of Heat and Mass Transfer 72 (2014) 622–629. doi:10.1016/j.ijheatmasstransfer.2014.01.038.
URL https://linkinghub.elsevier.com/retrieve/pii/S0017931014000660

[11] E. Solai, M. Guadagnini, H. Beaugendre, R. Daccord, P. Congedo, Lithium-ion batteries immersion cooling experiment, Mendeley Data (2021). doi:10.17632/2nf557wdyk.1.
URL https://data.mendeley.com/datasets/2nf557wdyk/1

[12] M. Shahjalal, T. Shams, M. E. Islam, W. Alam, M. Modak, S. B. Hossain, V. Ramadesigan, M. R. Ahmed, H. Ahmed, A. Iqbal, A review of thermal management for Li-ion batteries: Prospects, challenges, and issues, Journal of Energy Storage 39 (2021) 102518. doi:10.1016/j.est.2021.102518.
URL https://linkinghub.elsevier.com/retrieve/pii/S2352152X21002668

[13] R. Mahamud, C. Park, Reciprocating air flow for Li-ion battery thermal management to improve temperature uniformity, Journal of Power Sources 196 (13) (2011) 5685–5696. doi:10.1016/j.jpowsour.2011.02.076.
URL https://linkinghub.elsevier.com/retrieve/pii/S0378775311005039

[14] D. Chalise, K. Shah, R. Prasher, A. Jain, Conjugate Heat Transfer Analysis of Thermal Management of a Li-Ion Battery Pack, Journal of Electrochemical Energy Conversion and Storage 15 (1) (2018) 011008. doi:10.1115/1.4038258.
URL https://asmedigitalcollection.asme.org/electrochemical/article/doi/10.1115/1.4038258/444019/Conjugate-Heat-Transfer-Analysis-of-Thermal

[15] R. Camilleri, M. Sawani, Prediction of the Heat Transfer Coefficient in Direct Oil Cooling of Lithium-Ion Batteries, in: 2018 5th International Symposium on Environment-Friendly Energies and Applications (EFEA), IEEE, Rome, 2018, pp. 1–6. doi:10.1109/EFEA.2018.8617101.
URL https://ieeexplore.ieee.org/document/8617101/

[16] R.-D. Jilte, R. Kumar, Numerical investigation on cooling performance of li-ion battery thermal management system at high galvanostatic discharge, Engineering Science and technology, an International Journal (2018). doi:https://doi.org/10.1016/j.jestch.2018.07.015.

[17] L. Fan, J. Khodadadi, A. Pesaran, A parametric study on thermal management of an air-cooled lithium-ion battery module for plug-in hybrid electric vehicles, Journal of Power Sources 238 (2013) 301–312. doi:10.1016/j.jpowsour.2013.03.050.
URL https://linkinghub.elsevier.com/retrieve/pii/S0378775313004412

[18] J. Jaguemont, M. Sokkeh, S. Hosen, L. Jin, G. Qiao, T. Kalogiannis, J. van Mierlo, 1D-Thermal Analysis and Electro-Thermal Modeling of Prismatic-Shape LTO and NMC Batteries, in: 2019 IEEE Vehicle Power and Propulsion Conference (VPPC), IEEE, Hanoi, Vietnam, 2019, pp. 1–5. doi:10.1109/VPPC46532.2019.8952187.
URL https://ieeexplore.ieee.org/document/8952187/

[19] M. A. Perez Estevez, S. Calligaro, O. Bottesi, C. Caligiuri, M. Renzi, An electro-thermal model and its electrical parameters estimation procedure in a lithium-ion battery cell, Energy 234 (2021) 121296. doi:10.1016/j.energy.2021.121296.
URL https://linkinghub.elsevier.com/retrieve/pii/S0360544221015449

[20] A. Amini, T. Özdemir, Ö. Ekici, S. Ç. Başlamışlı, M. Köksal, A thermal model for Li-ion batteries operating under dynamic conditions, Applied Thermal Engineering 185 (2021) 116338. doi:10.1016/j.applthermaleng.2020.116338.
URL https://linkinghub.elsevier.com/retrieve/pii/S1359431120338163

[21] M. Suresh Patil, J.-H. Seo, M.-Y. Lee, A novel dielectric fluid immersion cooling technology for Li-ion battery thermal management, Energy Conversion and Management 229 (2021) 113715. doi:10.1016/j.enconman.2020.113715.
URL https://linkinghub.elsevier.com/retrieve/pii/S0196890420312395

[22] K. Jithin, P. Rajesh, Numerical analysis of single-phase liquid immersion cooling for lithium-ion battery thermal management using different dielectric fluids, International Journal of Heat and Mass Transfer 188 (2022) 122608. doi:10.1016/j.ijheatmasstransfer.2022.122608.
URL https://linkinghub.elsevier.com/retrieve/pii/S0017931022000904

[23] S. Drake, D. Wetz, J. Ostanek, S. Miller, J. Heinzel, A. Jain, Measurement of anisotropic thermophysical properties of cylindrical Li-ion cells, Journal of Power Sources 252 (2014) 298–304. doi:10.1016/j.jpowsour.2013.11.107.
URL https://linkinghub.elsevier.com/retrieve/pii/S0378775313019502

[24] L. Wei, Z. Lu, F. Cao, L. Zhang, X. Yang, X. Yu, L. Jin, A comprehensive study on thermal conductivity of the lithium ion battery, International Journal of Energy Research (2020) er.5016doi:10.1002/er.5016.
URL https://onlinelibrary.wiley.com/doi/abs/10.1002/er.5016

[25] C.-C. Chang, S.-Y. Huang, W.-H. Chen, Thermal and solid electrolyte interphase characterization of lithium-ion battery, Energy 174 (2019) 999–1011. doi:https://doi.org/10.1016/j.energy.2019.03.007.
URL https://www.sciencedirect.com/science/article/pii/S0360544219304116

[26] C. Park, A. K. Jaura, Dynamic Thermal Model of Li-Ion Battery for Predictive Behavior in Hybrid and Fuel Cell Vehicles, in: SAE Technical Paper, 2003, pp. 2003–01–2286. doi:10.4271/2003-01-2286.
URL https://www.sae.org/content/2003-01-2286/

[27] N. Sato, Thermal behavior analysis of lithium-ion batteries for electric and hybrid vehicles, Journal of Power Sources (2001) 8.

[28] V. Esfahanian, S. Akbari, F. Chaychizadeh, H. Dehghandorost, Capacity Fade Analysis of Lithium-Ion Cells Utilizing Uncertainty Quantification Approach, preprint, ECSarXiv (Dec. 2019). doi:10.1149/osf.io/f692w.
URL https://osf.io/f692w

[29] M. Hadigol, K. Maute, A. Doostan, On Uncertainty Quantification of Lithium-ion Batteries: Application to an LiC_6LiCoO_2 cell, Journal of Power Sources (Sep. 2015). doi:10.1016/j.jpowsour.2015.09.060.
URL http://arxiv.org/abs/1505.07776

[30] V. Laue, O. Schmidt, H. Dreger, X. Xie, F. Roder, R. Schenkendorf, A. Kwade, U. Krewer, Model-based uncertainty quantification for the product properties of lithium-ion batteries, Energy Technology 8 (2) (2020) 1900201. doi:https://doi.org/10.1002/ente.201900201.

[31] C. Andrew, A. Anirudh, C. Andrea, R. Giorgio, O. Simona, Stochastic capacity loss and remaining useful life models for lithium-ion batteries in plug-in hybrid electric vehicles, Journal of Power Sources 478 (2020) 228991. doi:https://doi.org/10.1016/j.jpowsour.2020.228991.
URL https://www.sciencedirect.com/science/article/pii/S037877532031288X

[32] W. Tong, W. Q. Koh, E. Birgersson, A. S. Mujumdar, C. Yap, Correlating uncertainties of a lithium-ion battery - A Monte Carlo simulation: A Monte Carlo simulation of a lithium-ion battery model, International Journal of Energy Research 39 (6) (2015) 778–788. doi:10.1002/er.3282.
URL http://doi.wiley.com/10.1002/er.3282

[33] J. Chen, J. E, S. Kang, X. Zhao, H. Zhu, Y. Deng, Q. Peng, Z. Zhang, Modeling and characterization of the mass transfer and thermal mechanics of the power lithium manganate battery under charging process, Energy 187 (2019) 115924. doi:https://doi.org/10.1016/j.energy.2019.115924.
URL https://www.sciencedirect.com/science/article/pii/S0360544219316081

[34] E. W. Lemmon, , I. H. Bell, M. L. Huber, M. O. McLinden, NIST Standard Reference Database 23: Reference Fluid Thermodynamic and Transport Properties-REFPROP, Version 10.0, National Institute of Standards and Technology (2018). doi:https://doi.org/10.18434/T4/1502528.
URL https://www.nist.gov/srd/refprop

[35] H. He, R. Xiong, J. Fan, Evaluation of lithium-ion battery equivalent circuit models for state of charge estimation by an experimental approach, Energies 4 (4) (2011) 582–598. doi:10.3390/en4040582.
URL https://www.mdpi.com/1996-1073/4/4/582

[36] L. H. Saw, Y. Ye, A. A. Tay, W. T. Chong, S. H. Kuan, M. C. Yew, Computational fluid dynamic and thermal analysis of Lithium-ion battery pack with air cooling, Applied Energy 177 (2016) 783–792. doi:10.1016/j.apenergy.2016.05.122.
URL https://linkinghub.elsevier.com/retrieve/pii/S0306261916307279

[37] G. Karimi, X. Li, Thermal management of lithium-ion batteries for electric vehicles, International Journal of Energy Research 37 (1) (2013) 13–24. doi:10.1002/er.1956.
URL http://doi.wiley.com/10.1002/er.1956

[38] Y. Li, L. Wang, C. Liao, Wu Lingfei, Li Junfeng, Guo Yanjie, Effects of temperature on dynamic characteristics of li-ion batteries in electric vehicle applications, in: 2014 IEEE

Conference and Expo Transportation Electrification Asia-Pacific (ITEC Asia-Pacific), IEEE, Beijing, China, 2014, pp. 1–6. doi:10.1109/ITEC-AP.2014.6940648.
URL http://ieeexplore.ieee.org/document/6940648/

[39] X. Li, C. Yuan, X. Li, Z. Wang, State of health estimation for li-ion battery using incremental capacity analysis and gaussian process regression, Energy 190 (2020) 116467. doi:https://doi.org/10.1016/j.energy.2019.116467.
URL https://www.sciencedirect.com/science/article/pii/S0360544219321620

[40] C. Lu, L. Zhang, J. Ma, Z. Chen, L. Tao, Y. Su, J. Chong, H. Jin, Y. Lin, Li-ion battery capacity cycling fading dynamics cognition: A stochastic approach, Energy 137 (2017) 251–259. doi:https://doi.org/10.1016/j.energy.2017.06.167.
URL https://www.sciencedirect.com/science/article/pii/S0360544217311623

[41] C. Rasmussen, Gaussian Process for Machine Learning, The MIT Press, 2006, massachusets Institute of Technology.

[42] D. G. Krige, A statistical approach to some mine valuation and allied problems on the Witwatersrand, Ph.D. thesis, Univ. of the Witwatersrand, Johannesburg (1951).

[43] J. Helton, F. Davis, Latin hypercube sampling and the propagation of uncertainty in analyses of complex systems, Reliability Engineering & System Safety 81 (1) (2003) 23–69. doi:10.1016/S0951-8320(03)00058-9.
URL https://linkinghub.elsevier.com/retrieve/pii/S0951832003000589

[44] M. C. Kennedy, A. OHagan, Bayesian calibration of computer models, Journal of the Royal Statistical Society: Series B (Statistical Methodology) 63 (3) (2001) 425–464. doi:10.1111/1467-9868.00294.
URL http://doi.wiley.com/10.1111/1467-9868.00294

[45] J. S. Liu, Monte Carlo Strategies in Scientific Computing, Springer Publishing Company, Incorporated, 2008.

[46] C. Robert, G. Casella, Monte Carlo Statistical Methods. 2nd ed, Springer-Verlag, New York, 2008.

[47] H. Heikki, S. Eero, T. Johanna, An adaptive metropolis algorithm, Bernoulli 7 (2) (2001) 223–242.
URL http://www.jstor.org/stable/3318737

[48] W. Chen, R. Jin, A. Sudjianto, Analytical Variance-Based Global Sensitivity Analysis in Simulation-Based Design Under Uncertainty, Journal of Mechanical Design 127 (5) (2004) 875–886. doi:10.1115/1.1904642.
URL https://doi.org/10.1115/1.1904642

[49] T. Sullivan, Introduction to Uncertainty Quantification, Springer, 2015, mathematics Institute University of Warwick.

[50] I. M. Sobol, Global sensitivity indices for nonlinear mathematical models and their Monte Carlo estimates, Mathematics and Computers in Simulation 55 (1) (2001) 271–280. doi:https://doi.org/10.1016/S0378-4754(00)00270-6.
URL https://www.sciencedirect.com/science/article/pii/S0378475400002706

[51] Y. Chen, X. Liu, G. Yang, H. Geng, An internal resistance estimation method of lithium-ion batteries with constant current tests considering thermal effect, in: IECON 2017 - 43rd Annual Conference of the IEEE Industrial Electronics Society, IEEE, Beijing, 2017, pp. 7629–7634. doi:10.1109/IECON.2017.8217337.
URL http://ieeexplore.ieee.org/document/8217337/